Received 26 March 2026; revised 23 May 2026; accepted 23 June 2026. Date of publication 29 June 2026;
date of current version 17 July 2026.

Digital Object Identifier 10.1109/OJIA.2026.3708024

Enhanced Discrete-Time Differentiators for *LCL* Resonance Damping Through Capacitor Voltage Feedback

JOSÉ DE ARIMATÉIA OLIMPIO FILHO [1], PAULO FERNANDO SILVA [1], LUIS DE ORO ARENAS [1], TIAGO DAVI CURI BUSARELLO [2] (Senior Member, IEEE), MARCELO GODOY SIMÕES [3] (Fellow, IEEE), AND HELMO KELIS MORALES PAREDES [1] (Senior Member, IEEE)

[1]São Paulo State University (UNESP), Institute of Science and Technology of Sorocaba, Sorocaba 18087-180, Brazil
[2]Department of Control, Automation and Computing Engineering, Federal University of Santa Catarina, Blumenau 89065-300, Brazil
[3]School of Technology and Innovations, University of Vaasa, 65101 Vaasa, Finland

CORRESPONDING AUTHOR: JOSÉ DE ARIMATÉIA OLIMPIO FILHO (e-mail: jose.olimpio@unesp.br)

This work was supported in part by the São Paulo Research Foundation (FAPESP) under Grant 2022/07811-3 and Grant 2022/15423-3, in part by the National Council for Scientific and Technological Development (CNPq) under Grant 304018/2025-2, and in part by the Coordination for the Improvement of Higher Education Personnel (CAPES) —Finance Code 001 and ROR identifier: 00x0ma614.

ABSTRACT The capacitor current active damping method is widely used to dampen the *LCL*-filter resonance in grid-connected inverters due to its simple implementation. Alternatively, it can be replaced by the capacitor voltage active damping (CVAD) as a low-cost solution, utilizing the capacitor voltage of *LCL*-filter for synchronization and damping, avoiding an extra sensor. A critical part of CVAD is the differentiator that is used to estimate capacitor current, yet, differentiators bring challenges due to their sensitivity to noise. To address these challenges, this article proposes a family of enhanced discrete-time differentiators—Lanczos, Super Lanczos 1, and Super Lanczos 2—for CVAD. This class of discrete-time differentiators based on finite impulse response filters is discussed, with detailed explanations provided on how to obtain the coefficients of the differentiators. The system was implemented using controller hardware-in-the-loop and experimental results demonstrate the effectiveness of the proposed method in damping the *LCL* resonance in a single-phase grid-connected inverter under steady state, under reference step conditions, and in the presence of noise.

INDEX TERMS Active damping (AD), capacitor voltage, digital differentiator, *LCL*-filter.

I. INTRODUCTION

Differentiators play a central role in both industrial and academic control applications, particularly in power electronic interfaces, such as grid-connected inverters (GCI) [1], [2], [3], [4], [5]. On the other hand, the differentiator inherently amplifies noise and adds phase error during the discretization process, which tends to adversely affect the GCI control strategy [3]. For this reason, several efforts in the literature have been focused on designing new differentiators with reduced noise amplification for capacitor voltage active damping (CVAD) of *LCL* filter resonance in GCIs [2].

The implementation of the digital derivative is carried out either by direct discretization of the ideal "*s*" function or indirectly through an approximate filter function [2], [6], [7].

Among conventional implementations of the differential element, represented in the z-domain, i.e., forward Euler, backward Euler (BE), and Tustin methods, only the BE is recommended [4], which provides better magnitude matching than the Tustin method, but results in a -90° phase shift at the Nyquist frequency, which leads to a significant phase delay and, consequently, affects the accuracy of the differentiator [1].

The indirect approach is implemented through a digital filter capable of replicating the frequency response of the ideal derivative term around an operating point [3]. The high-pass filter approximates the behavior of the "*s*" function below its cutoff frequency [8], [9]. Nevertheless, in high-frequency components, this structure introduces significant phase lag and adds extra hardware considerations [4].

TABLE 1. Comparative Analysis of Digital Differentiators

Criterion	BE [6]	HPF [8]	LLF [10]	nGI [1]	LF
Noise attenuation	No	Medium	Low	Medium	Medium
Simplicity	Higher	Good	Good	Low	Good
Direct discrete form	Yes	No	No	No	Yes
Effective frequency	Low	Low	Narrow	Wide	Medium
Order	First	First	First	Second	Higher

The lead-lag filter (LLF) element is another common approach [10]; however, its operation is limited to a narrow frequency range, resulting in a slight phase deviation from the desired 90°. This method also exhibits low robustness to parametric variations because its tuning is based on the filter's resonance frequency, which is sensitive to different feeder impedance conditions [1]. The quadrature-second-order generalized integrator [1] exhibits similar behavior to the LLF, but, it guarantees zero phase delay at the desired frequency. A drawback is that its derivative is only effective over a narrow range [11]. An adjustable differentiator based on the generalized integrator, both ideal (GI) and nonideal (nGI), was introduced in [1], with its magnitude and phase conveniently designed for differentiation.

According to [12], the nGI has proven to be one of the main methods for highly accurate derivative emulation. This approach mimics the "*s*" function across the entire frequency range; however, it introduces complexity into the tuning process and the undesirable characteristic of amplifying high-frequency components of the feedback signal [13]. Moreover, the nGI depends on a trade-off between noise amplification and phase error due to the damping factor. A higher damping factor increases noise rejection capability, nevertheless, it is penalized by a larger phase error. Conversely, a lower damping factor brings the performance closer to the ideal derivative, but it results in a noisier signal [2]. In [2], two digital differentiators are proposed, directly developed in the discrete domain, which are a first-order backward-lead differentiator, and a second-order differentiator that combines the Tustin differentiator with a digital notch filter, whose fundamental concept involves adjusting the frequency responses to align with the "*s*" function with embedded filters [3]. The two methods present simple expressions, given by their direct discrete nature, and share the same derivative characteristics as the nGI [14].

The discrete-time optimal control-based tracking differentiator (fHan-TD) [15] offers high noise attenuation, which makes it frequently used in active disturbance rejection control to meet a transient profile. Like other differentiators, the fHan-TD involves a tradeoff between noise attenuation and phase delay [3]. Huang et al. [3] proposed a novel reduced-order generalized differentiator, which achieves good differentiation properties with zero phase delay and simultaneously improves noise attenuation. Nevertheless, the main drawback is its nontrivial and complex design methodology. In [16], a model-free and robust trapezoidal method-based high-gain tracking differentiator is proposed to extract differential signals and mitigate the impact of time delay in the point of common coupling (PCC) voltage feedforward. Still, this approach involves a tradeoff between phase lag and noise suppression.

To overcome the aforementioned drawbacks, this article proposes the application of a new resonance active damping (AD) strategy based on high-frequency differentiators by applying the Lanczos, super Lanczos 1 (SL1), and super Lanczos 2 (SL2) techniques, here called the Lanczos family (LF). These differentiators are attractive due to their simplicity, low computational cost and can be applied to inherently noisy signals, producing a smoothing effect at each new sample. In addition, they offer superior matching bandwidth compared to traditional differentiators. They also exhibit low gain at high frequencies, which reduces sensitivity to noise. They have a narrow-band characteristic, as their frequency response matches that of the ideal differentiator only at low frequencies [17].

The concept of this family of differentiators is explained in [18] and [19] and has been used in biomedical systems [20], power systems [21], and sensorless electric drive systems [22], [23]. It is noteworthy that the differentiation characteristics and accuracy have not been discussed in the literature for *LCL* filter resonance damping strategies in GCIs. In this case, the capacitor-voltage-based AD employs a sinusoidal signal, characterized by continuous and smooth variation without discontinuities, which results in a more predictable frequency-domain behavior and reduced harmonic content. Consequently, the analyzes and applications associated with sinusoidal signals differ from those involving sawtooth-type signals, both in terms of modeling and filtering as well as in the design of controllers and differentiators, thus constituting an innovation and an alternative solution compared to traditional techniques. The main difference from [22], [23] lies in the fact that the derived signal exhibits a sawtooth waveform. This type of signal presents a linear time variation; however, it features an abrupt discontinuity at the waveform peak, i.e., during the transition from the rising to the falling slope, which results in high harmonic components and increased susceptibility to noise and saturation in the practical implementation of the differentiator. Table 1 summarizes the review of the literature on the state-of-the-art differentiators for CVAD in GCI, highlighting comparative analyzes.

In this regard, this article addresses the development of a tuning methodology for high-frequency differentiators based on LF, the derivation of compact expressions for digital implementation in digital signal controllers (DSC), and the preservation of simplicity and low computational cost while improving robustness to noise, provides contributions to discrete-time differentiators, offering superior performance compared to conventional methods for AD strategies. The main contributions of this article are as follows.

1) A detailed tuning methodology for the high-frequency differentiators, based on Lanczos and SL1 and SL2 techniques, for computing CVAD in GCI, achieving greater accuracy in derivative extraction and improved noise rejection.
2) A set of compact difference equations suitable for digital implementation of the derivative in DSC, which facilitate their implementation in real-world applications.
3) This approach preserves the simplicity and low computational cost characteristic of derivative-based algorithms, while simultaneously improving their robustness to noise.
4) The effectiveness of the proposed differentiator is verified through controller hardware-in-the-loop (C-HIL) testing and experiments in a laboratory scale prototype, allowing modifications of system parameters in real time and thus evaluating the performance of the CVAD.

The rest of this article is organized as follows. Family of differentiators applied for CVAD is described in Section II. Section III presents a performance analysis of these elements based on different figures of merit. A brief review modeling of the *LCL* type GCI in Section IV. Experimental results are carried out in Section V. Finally, Section VI concludes this article.

II. DIFFERENTIATORS BASED ON FIR FILTERS

This section presents considerations on discrete-time differentiators from the LF, along with simple and widely discussed discrete-time differentiators found in the literature. It is emphasized that these differentiators behave similarly to ideal differentiators within the application range of the CVAD technique.

A. THEORETICAL BASIS OF DIGITAL DIFFERENTIATION

Differentiation is a mathematical operation used in continuous systems and often adopted in discrete-time systems. However, the ideal differentiator cannot be directly implemented in discrete-time applications, as it has an infinite and noncausal impulse response, requiring approximation to a causal and finite impulse response (FIR) [17].

It is important to note that derived signals are prone to accurate issues, such as phase error and noise pollution, which can destabilize the GCI control, particularly in inverter-based applications, when the *LCL* filter cannot adequately attenuate switching harmonics. Therefore, the discrete derivative is emulated by digital filters that mimic the differentiator's behavior in the frequency range of interest (low frequencies), while providing high attenuation at high frequencies [24].

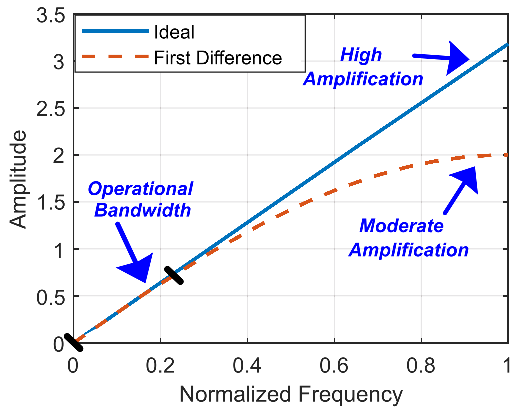

FIGURE 1. Comparison: continuous-time ideal differentiator versus digital filter as differentiator.

Fig. 1 depicts this concept, illustrating a comparison between a "*s*" function and a digital filter working as a digital differentiator. Although the concept of a matching band is not typically addressed in digital signal processing, it becomes relevant in the context of differentiator filters. Unlike conventional filters, ideal differentiators exhibit a gain that increases monotonically with frequency. Therefore, this concept is introduced and discussed in the following section.

B. DIFFERENTIATOR COINCIDENCE RANGE

The concept of a coincidence region or matching band for differentiator filters is essential, as these filters ideally exhibit increasing gain with frequency and do not have a well-defined passband or stopband. Noise typically arises over a wide range of frequencies; but it is more prominent at high frequencies in digital systems, contributing to significant amplification in continuous-time differentiators. In this respect, differentiator filters have an advantage, as they mimic the behavior of ideal differentiators within a limited region called the coincidence region (linear range). However, unlike the ideal differentiator, they attenuate high-frequency signals, enabling applications that rely on differentiation in noisy signals [23].

Therefore, in the coincidence range shown in Fig. 1, the matching band corresponds to the frequency range of a differentiator filter that aligns with the response of an ideal differentiator of the same order, with only a slight gain deviation [25].

It is emphasized that, for proper digital implementation of a derivative function, the signal to be differentiated must have its frequency range confined within the operational bandwidth of the differentiator. In this region, the differentiation operation of a given input signal is performed accurately and robustly, while outside this region, noise-polluted signals are

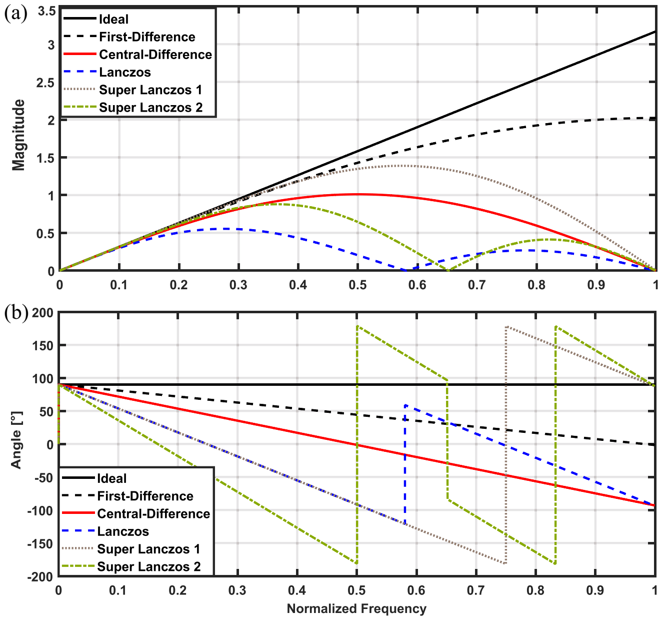

FIGURE 2. **Frequency responses for enhanced discrete-time differentiators. (a) Magnitude. (b) Phase.**

smoothed. Therefore, it is crucial that the bandwidth of the analyzed signal fit within this region to ensure that the discrete derivative is performed efficiently [22].

C. SIMPLE DISCRETE-TIME DIFFERENTIATORS

Signal differentiation is a common task used to compute derivatives of discrete-time signals. The first-difference (FD) differentiator, denoted by $y_{\mathrm{FD}}[k]$, calculates the difference between successive samples of the signal $x[k]$, as described by (1), with the sampling period omitted for convenience. While its implementation is straightforward, the FD differentiator tends to amplify noise, which propagates into the output signal, as shown in its frequency response in Fig. 2(a)

$$y_{\mathrm{FD}}[k] = x[k] - x[k-1]. \tag{1}$$

Using Lagrange's interpolation polynomials, several methods of numerical differentiation were developed based on central difference (CD), whose the general form is in the following equation [20]:

$$f'(x_0) \approx \frac{1}{h} \sum_{k=1}^{(N-1)/2} a_k \left(f_k - f_{-k}\right) \tag{2}$$

where x_0 is the point of interest, N is the total number of points used (odd), $f_{\pm k}$ represents $f(x_0 \pm kh)$, and a_k are the parameters to be determined.

The CD differentiator, $y_{\mathrm{CD}}[k]$, as described in (3), is derived by taking the difference between two consecutive samples of the signal, which results in noise attenuation due to its low-pass filter characteristics. For this reason, CD is commonly used in practical applications. However, the drawback of this method is amplification of noise and a limited frequency range of linear operation, which is narrower than that of the FD differentiator [26]

$$y_{\mathrm{CD}}[k] = \frac{x[k] - x[k-2]}{2}. \tag{3}$$

Thus, it is essential to develop computationally efficient differentiators that retain the high-frequency attenuation benefits of the CD differentiator while expanding its linear frequency range [19]. To address this gap, the proposed enhanced differentiators are based on the CD and Hamming differentiators, known as low-noise Lanczos filters, $y_L[k]$, SL1, y_{SL1} [k], and SL2, y_{SL2} [k].

Lanczos presents this technique to develop a polynomial interpolation technique for discrete functions. Moreover, these differentiators are inherently FIR filters, making them suitable for low-cost and low-power applications [20]. Therefore, they are always stable, their implementation is straightforward [27]. For classical FIR filters, their design essentially involves defining the filter order and obtaining its coefficients. This is achieved by the window method and then applying the inverse discrete Fourier transform, as follows:

$$h[k] = \frac{1}{N} \sum_{n=0}^{N-1} H(m)\, e^{j\frac{2\pi nk}{N}} \tag{4}$$

where $h[k]$ is the coefficients vector of the discrete-time differentiator, N is the size of the window, $H(m)$ is the discrete sequence that describes the desired frequency response, and n and m are indexes in discrete-time domain and discrete frequency domain, respectively [23].

In summary, the design of the differentiators consists of locally approximating the analyzed function, $f(x)$, by a polynomial of degree M. Thus, signal filtering is performed through polynomial approximation [28]

$$P_M(x) = \sum_{j=0}^{M} a_j x^j. \tag{5}$$

Subsequently, the metric based on the mean-squared error in (6) is minimized, such that the unknown coefficients a_j are obtained as the solution of a linear system of equations [20]

$$Z = \sum_{k=-(N-1)/2}^{(N-1)/2} \left(f_k - P_M(x_k)\right)^2. \tag{6}$$

Finally, with the aid of the computed polynomial, $f'(x_0)$ can be estimated as in (7). Further details are provided in [18]

$$f'(x_0) = P'_M(x_0). \tag{7}$$

On the other hand, the Lanczos differentiator is derived by fitting a second-order polynomial to five consecutive samples using a least squares (LSs) criterion. By minimizing the sum of squared differences between the curve and the data, the coefficients of the Lanczos differentiator can be obtained. This is achieved by taking the partial derivative of the LS function and setting it to zero to get the final coefficients.

The SL1 method focuses on matching an FIR filter to an ideal differentiator in the frequency domain by using a Taylor series expansion of the filter's frequency response and sets specific constraints to ensure the first term equals one for differentiation and the second term equals zero for noise filtering. In contrast, SL2 extends the original Lanczos approach by fitting a third-order polynomial to seven consecutive samples. This involves solving a system of equations derived from partial derivatives with respect to two coefficients to determine the set of filter coefficients.

Based on the previous considerations, the difference equations for the Lanczos, $y_L[k]$, SL1, $y_{\mathrm{SL1}}[k]$, and SL2, $y_{\mathrm{SL2}}[k]$, differentiators are obtained and given by (8), (9), and (10), respectively. It is also noted that the central coefficient is zero for the Lanczos, SL1, and SL2 schemes [19]. The Appendix presents all the steps required to determine the coefficients of these differentiators

$$y_L[k] = \frac{1}{5}x[k] + \frac{1}{10}x[k-1] - \frac{1}{10}x[k-3] - \frac{1}{5}x[k-4] \tag{8}$$

$$\begin{aligned} y_{\mathrm{SL1}}[k] = &-\frac{1}{12}x[k] + \frac{8}{12}x[k-1] \\ &-\frac{8}{12}x[k-3] + \frac{1}{12}x[k-4] \end{aligned} \tag{9}$$

$$\begin{aligned} y_{\mathrm{SL2}}[k] = &-\frac{22}{252}x[k] + \frac{67}{252}x[k-1] + \frac{58}{252}x[k-2] \\ &-\frac{58}{252}x[k-4] - \frac{67}{252}x[k-5] + \frac{22}{252}x[k-6]. \end{aligned} \tag{10}$$

Fig. 2(a) compares the amplitude response of the ideal differentiator, FD, CD, Lanczos, SL1, and SL2 structures. The frequency axis is normalized with respect to $f_s/2$, where f_s is the sampling frequency. The accuracy of the differentiators is high within a certain matching band. As observed from the Fig. 2, the FD differentiator most closely approximates the ideal magnitude response, exhibiting the largest region of coincidence with the ideal differentiator. However, it also shows high magnitude at high frequencies (above f=0.5 $f_s/2$). In practical applications, this can be disadvantageous, as the differentiator may amplify high-frequency noise [17]. It should be noted that, unlike ideal differentiators, practical digital differentiators are designed to exhibit low-pass magnitude response characteristics, since they behave as differentiators only up to a certain cutoff frequency, beyond which higher frequency components are attenuated, thereby rejecting high-frequency noise and reducing its impact [29].

Fig. 2(b) shows the phase response of the analyzed differentiators. These curves are plotted with limits varying from $-\pi$ to π, which explains the observed discontinuities. The curves clearly reflect the natural behavior of FIR filters, with differences in slope. The ideal differentiator exhibits a null phase shift because the phase is normalized at $\pi/2$, by convention, the output signal of the ideal differentiator introduces a $\pi/2$ phase shift relative to the input signal, valid across all frequencies, implying the absence of phase distortion and zero phase delay. In contrast, the other differentiators induce a phase shift that depends on the signal frequency input.

TABLE 2. Effective Time Delay Introduced by the Evaluated Differentiators

Differentiator	Δt_ϕ (μs)
FD	11
CD	11.1
Lanczos	22
SL1	22
SL2	33.4

It is worth noting that the FD exhibits a nonlinear phase and, consequently, a frequency-dependent phase delay, which leads to temporal distortions. In contrast, the CD and the Lanczos differentiator present an approximately constant phase delay only at low and mid frequencies, whereas the super Lanczos differentiators preserve this property more consistently within the design bandwidth due to their frequency-response sampling-based synthesis method. The apparent "jumps" observed in the phase curves arise from the phase wrapping phenomenon, which results from limiting the phase to the interval $[-\pi, \pi]$. Such discontinuities correspond to integer multiples of 2π and do not affect the effective phase delay of the filter; they vanish when the phase is unwrapped, revealing an almost linear behavior within the frequency band of interest.

Ideally, differentiators should be designed to operate at these frequencies to match the phase behavior of the ideal differentiator. Alternatively, they can be designed for any frequency, but this requires angle compensation techniques, which are beyond the scope of this article. It is noteworthy that, at a frequency of 60 Hz, the point lies near the origin of the coordinate plane; therefore, all differentiators exhibit nearly the same phase response.

III. PERFORMANCE INDICES OF DIFFERENTIATORS

In this section, a comparative analysis of the performance of the proposed differentiators is presented, utilizing various numerical and graphical metrics. This approach provides a more detailed and accurate assessment, facilitating the selection of the most suitable differentiator for each specific application. Further details regarding the different figures of merit are presented as follows.

A. TIME DELAY

To evaluate the impact of time delay (Δt_ϕ) and amplitude (Δy) associated with the differentiators designed in Section II, the respective analysis results are presented in Fig. 3 and Table 2. In this case, a resistive–capacitive (RC) circuit with a sinusoidal input signal of 127 $\mathrm{V_{RMS}}$ at 1 kHz, around the control system bandwidth, was used to compare the estimated capacitor current (i_{C_f}) obtained via the FIR filter described in Section II with its actual measured value ($i^*_{C_f}$), directly acquired from the capacitive branch of the RC circuit using the

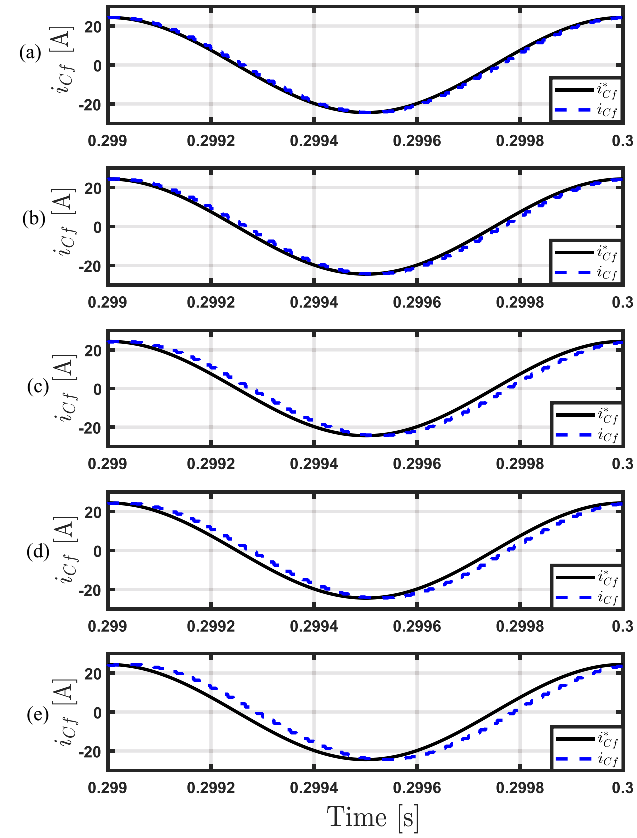

FIGURE 3. Time-delay analysis of the evaluated differentiators. (a) FD. (b) CD. (c) Lanczos. (d) SL1. (e) SL2.

PSIM[1] software. The sampling frequency was set to 90 kHz, and further details are discussed in [11].

It is observed that these differentiators exhibit excellent performance in approximating the magnitude frequency response of an ideal differentiator, as shown in Fig. 3. However, higher order filters, such as SL2, introduce an increased time delay, which results in additional delay in the system and may be detrimental to the performance of capacitor current estimation. These results are quantified in Table 2. The effective delay increases from approximately 11 μs for FD and CD to 22 μs for Lanczos and SL1, reaching 33.4 μs for SL2. Consequently, the attenuation of the resonance peak can be compromised, posing a risk of performance degradation and potentially leading to system instability. Furthermore, in the case of CVAD, time delay compensation is not required. Note that, for other sampling frequencies, the delay effects should be evaluated again, since changes in the sampling rate may significantly influence the phase response and overall system performance.

B. PERFORMANCE INDICES

For better quantitative and qualitative interpretation of differentiators, some error-based performance indices for control analysis were used, namely: integral absolute error (IAE), integral of time multiplied absolute error (ITAE), integral squared error (ISE), and integral of time multiplied squared error (ITSE) [30]. These performance indices are represented in (11), (12), (13), and (14), respectively. For these indices, the error is measured as the difference between the current measured directly in the RC circuit and the current estimated via the derivative of the voltage.

The IAE is evaluated based on the magnitude of the error, disregarding its duration or persistence. IAE and ITAE consider the absolute value of the error, while ISE and ITSE consider the squared error. In addition, ISE is similar to IAE, but the error is squared. Finally, ITSE and ITAE incorporate the error multiplied by time; however, in ITSE, the error is squared, giving greater weight to larger errors in the steady state. These specific characteristics of each performance index highlight different aspects of the differentiator response. It is noted that (6) follows the same principle as the ISE/ITSE indices, as it is based on the minimization of the squared error, thus emphasizing larger deviations

$$\mathrm{IAE} = \int_0^{t_f} |x_{\mathrm{ref}}(t) - x(t)|\; dt \tag{11}$$

$$\mathrm{ISE} = \int_0^{t_f} (x_{\mathrm{ref}}(t) - x(t))^2\; dt \tag{12}$$

$$\mathrm{ITAE} = \int_0^{t_f} t\,|x_{\mathrm{ref}}(t) - x(t)|\; dt \tag{13}$$

$$\mathrm{ITSE} = \int_0^{t_f} t\,(x_{\mathrm{ref}}(t) - x(t))^2\; dt \tag{14}$$

where t_f is the final simulation time, x is the controlled variable, and x_{ref} is the reference.

Table 3 presents the performance indices of differentiators. The results demonstrate the superiority of the FD method, as it consistently exhibited lower values of IAE, ISE, ITAE, and ITSE across all scenarios. The CD method showed slightly higher performance indices compared to the FD method, with minimal differences observed in specific cases, such as ISE. Both Lanczos and SL1 exhibited intermediate and similar performance indices; however, they were higher compared to the previous methods. Finally, the SL2 case presented the worst performance indices when compared to the others.

TABLE 3. Error-Based Performance Indices Obtained for the Evaluated

Diff.	IAE$\times10^3$	ISE$\times10^3$	ITAE$\times10^3$	ITSE$\times10^3$
FD	3.3429	4.3395	0.1751	21.1110
CD	3.9222	4.3527	0.2629	31.5980
Lanczos	5.0821	4.3914	0.43857	65.2710
SL1	5.0824	4.4013	0.43859	65.2750
SL2	6.2437	4.4570	0.61425	115.8700

[1]Registered trademark

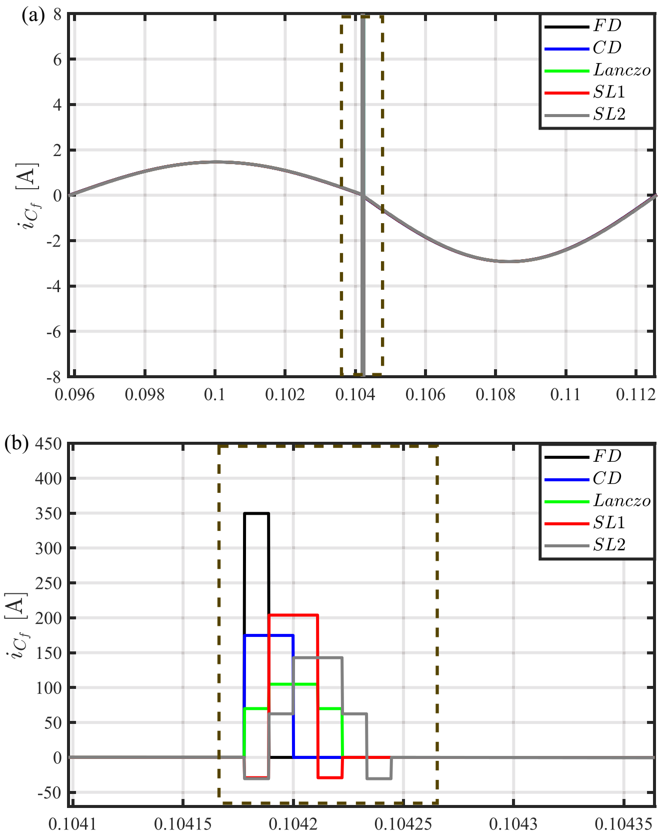

FIGURE 4. **Comparison of the differentiators. (a) Amplitude step test. (b) Zoomed view at the event instant.**

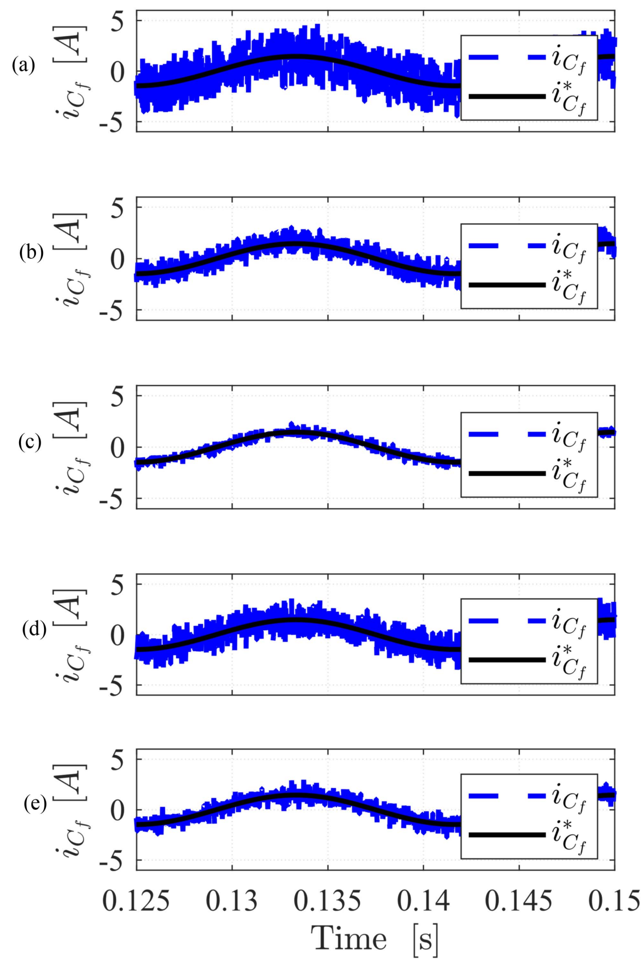

FIGURE 5. **Noise-sensitivity analysis of the evaluated differentiators. (a) FD. (b) CD. (c) Lanczos. (d) SL1. (e) SL2.**

C. STEP RESPONSE PERFORMANCE

To evaluate the dynamic behavior of the differentiators, a step response performance analysis was conducted with a 100% amplitude variation in the sinusoidal source at the instant 0.104167 s. The parameters analyzed were settling time and overshoot, as shown in Fig. 4. Fig. 4(a) presents the derived signal of a sinusoidal waveform subjected to a step at a given instant, with the results obtained for each of the analyzed differentiators. For this evaluation, the same RC circuit described in Section III-B was considered. In turn, Fig. 4(b) provides a zoomed-in view of this scenario, highlighting the impact of the step on the responses of the differentiators. It is noted that the FD exhibits the shortest settling time; however, it has the drawback of a more pronounced overshoot. The CD demonstrates similar settling behavior to the FD but with a lower overshoot. The SL1 shows intermediate behavior when compared to the others, while the SL2 exhibits the longest settling time but with a reduced overshoot. Finally, the Lanczos differentiator definitively offers the best cost-benefit ratio in this scenario.

The y-axis scaling in Fig. 4(b) is consistent with Fig. 4(a). However, the peak value was intentionally omitted in Fig. 4(a) to preserve waveform readability and emphasize the overall (steady state) sinusoidal behavior. In contrast, Fig. 4(b) highlights the transient effects introduced by the step variation, including response peaks and differences among the evaluated differentiators. This separation improves result interpretation by distinguishing the steady-state and transient g analyzes.

D. NOISE REJECTION

In this test, the influence of noise caused by effects such as converter switching, power supply, grid emulator source, among others, was considered. To quantify the noise, it was set as a random voltage source at 1% of the original signal value. An alternative approach based on the signal's power spectral density is seldom available in practice and relies on spectral assumptions that may not be representative, potentially failing to capture the dynamics of the differentiator [31]. Based on these considerations, the FD is the most prone to noise amplification, followed by the CD, which exhibits similar behavior to the SL1. The SL2 shows good noise immunity compared to the previous methods. Finally, it is noteworthy that the Lanczos differentiator demonstrates the best performance in noise rejection, as shown in Fig. 5.

TABLE 4. Comparisons of the Computational Resources

Diff.	Coefficients	Order Delay	Execution Time
FD	2	1	145 ns
CD	2	2	167 ns
Lanczos	4	4	260 ns
SL1	4	4	260 ns
SL2	6	6	330 ns

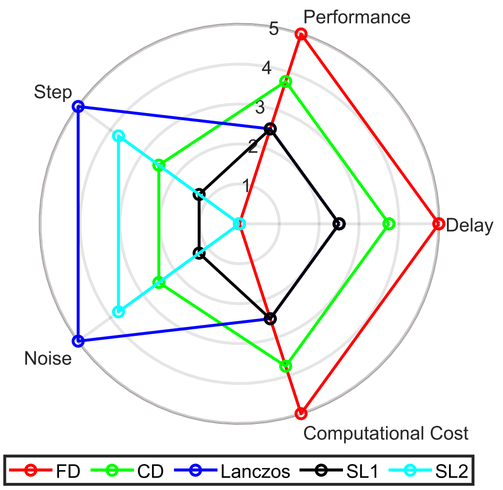

FIGURE 6. Qualitative radar-chart comparison of the evaluated differentiators based on normalized performance metrics.

E. COMPUTATIONAL COST

The computational cost of the differentiators is measured in relation to the number of mathematical expressions, digital delay, number of cycles required for differentiation, and the average execution time of the differentiators for each DSP cycle. The results are displayed in Table 4. It can be found that the FD differentiator not only uses fewer computational resources but also executes the algorithm in a faster way. It is observed that the Lanczos differentiator exhibits intermediate behavior, while the SL2 shows the highest computational cost.

Fig. 6 depicts radar chart of the differentiator. Each parameter has been normalized based on performance on a scale from 1 to 5, where a value of 1 represents the worst performance and 5 represents the best performance. When comparing the proposed differentiators, it becomes evident that there is a tradeoff between all of them. The SL2 ranks as the worst, presenting good dynamic robustness and noise immunity; however, it exhibits high delay, the worst overall performance, and higher computational cost. On the other hand, the FD and CD show intermediate behavior, with an emphasis on low computational cost and minimal phase delay. Finally, the Lanczos differentiator stands out for its best cost-benefit ratio, due to its excellent performance in the main metric, i.e., its noise rejection capability, combined with reduced phase delay and good performance under dynamic variations.

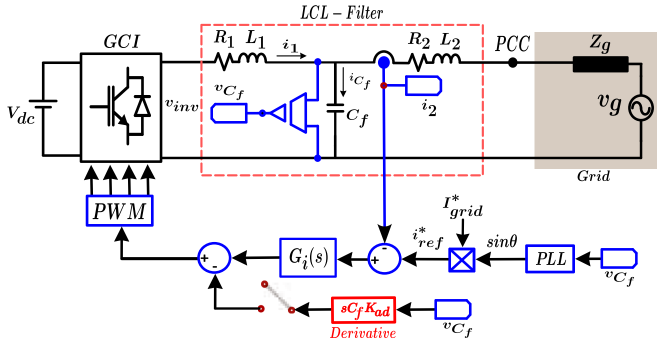

FIGURE 7. Schematic diagram of an *LCL* filter-connected single-phase inverter system to the grid.

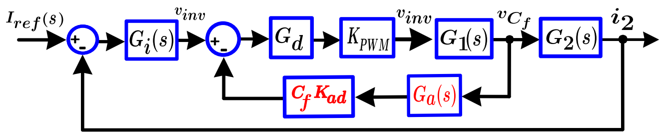

FIGURE 8. Block diagram of the control structure for CVAD of the GCI with the *LCL* filter.

IV. MODELING AND CONTROL STRATEGY FOR *LCL*-TYPE GCI

This section presents the modeling and the design of controller for the GCI.

A. TOPOLOGY OF THE GCI

Fig. 7 depicts the schematic diagram of a single-phase grid-connected system. A distributed energy resource, implemented as a DC power supply, is connected to the DC bus. In this way, the GCI operates with a constant DC-link voltage. The *LCL* filter consists of a converter-side inductor L_1, a filter capacitor C_f, a grid-side inductor L_2, and L_g represents the grid inductance at the PCC.

The variable i_1 is the output current on the inverter side, i_2 represents the output current on the grid side, and i_{C_f} represents the current through C_f. The grid current (i_2) is controlled, and the voltage of the capacitor, v_{C_f}, is sensed for both the CVAD and a phase-locked loop (PLL) to ensure grid synchronization. The term G_d represents PWM and computation delays, whose expression can be given by (15), where T_s is the sampling period [32]

$$G_d = e^{-1.5T_s s}. \tag{15}$$

To avoid an extra current sensing, i_{C_f} is estimated through the derivative of v_{C_f}, as shown in Fig. 7, where K_{ad} is the damping gain. The function relating the inverter bridge output voltage v_{inv} to the grid current i_2 is calculated by (16), where ω_r is the *LCL* filter resonance frequency, as expressed in (17). According to Fig. 8, the functions from v_{inv} to v_{C_f} and as well as the transfer function from $v_{\mathrm{C_f}}$ to i_2 are given as (18), respectively [1], [2]. Observe that G_a is a digital differentiator used to emulate the ideal "s" function, being valid only within the frequency range in which the differentiator accurately approximates the ideal derivative behavior

$$G_{i_2}(s) = \frac{i_2(s)}{v_{\text{inv}}(s)} = \frac{1}{(L_2+L_g)L_1C_f\, s\left(s^2+\omega_r^2\right)} \tag{16}$$

$$\omega_r = \sqrt{\frac{L_1+(L_2+L_g)}{L_1(L_2+L_g)C_f}} \tag{17}$$

$$G_1(s) = \frac{v_{C_f}(s)}{v_{\text{inv}}(s)} = \frac{1}{L_1C_f\left(s^2+\omega_r^2\right)} \tag{18}$$

$$G_2(s) = \frac{i_2(s)}{v_{C_f}(s)} = \frac{1}{s\left(L_2+L_g\right)}. \tag{19}$$

Since the LF differentiators are inherently implemented directly in the z-domain for the digital realization of the CVAD, zero-order hold discretization is applied to (16) and (18), according to the discrete model shown in Fig. 2(b), yielding (20) and (21), respectively [1], [2]

$$G_{i_2}(z) = \frac{\omega_r T_s\alpha - \sin(\omega_r T_s)\,(z-1)^2}{\omega_r\left(L_1+L_2+L_g\right)(z-1)\alpha} \tag{20}$$

$$G_{v_{C_f}}(z) = \frac{[1-\cos(\omega_r T_s)]\,(z+1)}{\omega_r^2 L_1 C_f\alpha} \tag{21}$$

$$\alpha = z^2 - 2z\cos(\omega_r T_s) + 1. \tag{22}$$

To eliminate the current steady-state error at the fundamental frequency ω_0, a proportional–resonant (PR) current controller, $G_i(s)$, is used, as given in (23), with a proportional gain K_p and a resonant gain K_i, defined by (24) and (25), respectively [33]

$$G_i(s) = K_p + K_i\frac{sB_r}{s^2+2\zeta B_r s+\omega_r^2} \tag{23}$$

$$k_p = \frac{(2\xi+1)\left(\sqrt{(2\xi+1)}\,\omega_r L_{\text{eq}} - R_{\text{eq}}\right)}{V_{\text{dc}}} \tag{24}$$

$$K_i = \frac{\omega_r^2 L_{\text{eq}}\left[(2\xi+1)^2-1\right]}{2V_{\text{dc}}} \tag{25}$$

where $L_{\text{eq}} = L_1 + L_2$, R_{eq} represents the sum of the resistances of the inductors of the *LCL* filter, ξ is the damping factor, ω_g is the grid angular resonant frequency, B_r is the resonant bandwidth in hertz, and ζ is the damping factor of the resonant filter. It is noteworthy that the discretized coefficients of the resonant filter in (17) are obtained by applying the Z-transform to the continuous-time transfer function, resulting in

$$H_r(z) = \frac{b_0 + b_1z^{-1} + b_2z^{-2}}{a_0 + a_1z^{-1} + a_2z^{-2}} \tag{26}$$

such as

$$b_0 = B_rT_s \tag{27}$$

$$b_1 = -B_re^{-0.5B_rT_s}\cos(T_s\omega_x - \gamma)\,T_s \tag{28}$$

$$b_2 = 0 \tag{29}$$

$$a_0 = 1 \tag{30}$$

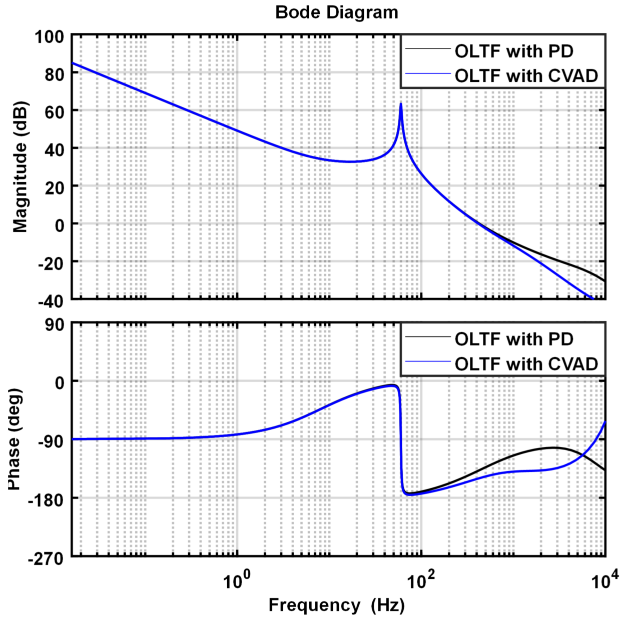

FIGURE 9. Frequency response of the compensated open-loop transfer function with CVAD and passive damping.

$$a_1 = -2e^{-0.5B_rT_s}\cos(T_s\omega_x) \tag{31}$$

$$\omega_x = \sqrt{\omega_g^2 - 0.25B_r^2} \tag{32}$$

$$\gamma = \frac{0.5B_r^2}{\sqrt{\omega_g^2-0.25B_r^2}}e^{-0.5B_rT_s}\sin(T_s\omega_x)\,. \tag{33}$$

It is important to ensure that the PR controller's bandwidth is at least ten times lower than the switching frequency. The value of B_r should be around 1.5 Hz and ζ any value between 0.1 and 1, where $\zeta = 0.5$ makes the resonant filter present 0 dB at the resonant frequency. Design details of the PR controller can be found in [33], and the designs of the damping gain K_{ad} have been intensively discussed in [34], thus, they are not repeated here.

Through these expressions, the open-loop transfer function considering the capacitor voltage feedback loop in the discrete domain, $T_{vz}(z)$, can be determined according to (34) [2]. Note that $G_a(z)$ represents the Lanczos differentiator, and that increasing the sampling frequency of the differentiator expands the range of coincidence, thereby making the approximation significantly more accurate and reliable

$$T_{vz}(z) = \frac{K_{\text{wpm}}G_i(z)G_{i2}(z)}{z + K_{ad}K_{\text{pwm}}C_fG_a(z)G_{vc_f}(z)}. \tag{34}$$

Therefore, Fig. 9 compares the frequency responses of the compensated open-loop transfer function with CVAD and traditional passive damping (PD) [34], the latter implemented by inserting a resistor in series with the capacitor, demonstrating similar performance within the target differentiation bandwidth.

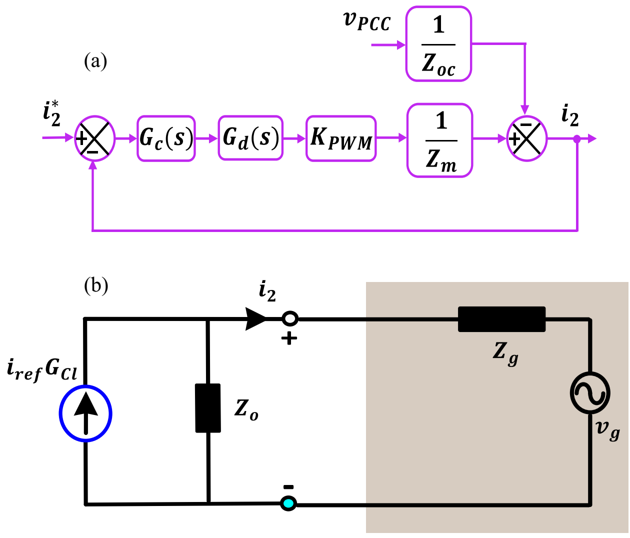

FIGURE 10. Equivalent representations used for impedance-based stability analysis. (a) Simplified control block diagram. (b) Norton equivalent circuit of the GCI.

B. ANALYSIS ON THE IMPEDANCE-BASED STABILITY

The inverter impedance model is employed to analyze the external stability of the GCI [35], [36], taking into account the interaction between the GCI and the power grid to which it is connected. This analysis highlights the influence of external factors, such as variations in the grid impedance. Ensuring external stability is essential to prevent oscillations in the injected current, mitigate waveform distortions, and avoid degradation of power quality, as well as instability in the converter [37].

In summary, the stability of the GCI is determined by the interaction between its output impedance, Z_o, and the grid impedance, Z_g. To facilitate the impedance analysis, the equivalent control diagram in Fig. 8 is simplified to yield the Norton equivalent circuit shown in Fig. 10(a) and the equivalent circuit model is shown in Fig. 10(b) [38].

With the aid of Fig. 10(b), the transfer functions relating the grid-injected current to the inverter output voltage, $Y_m(s)$, as well as the grid-injected current to the PCC voltage, $Y_{oc}(s)$, are derived and given by (35) and (36), respectively [39]

$$Y_m(s) = \frac{1}{L_1 L_2 C s^3 + L_2 G_d K_{PWM} K_{ad} G_a s + (L_1 + L_2)s} \tag{35}$$

$$Y_{oc}(s) = \frac{L_1 C s^2 + 1 + G_d K_{PWM} K_{ad} s}{L_1 L_2 C s^3 + L_2 G_d K_{PWM} K_{ad} G_a s + (L_1 + L_2)s}. \tag{36}$$

Therefore, the grid current can be expressed as a function of the closed-loop transfer function, G_{cl}, and inverter output admittance, $Z_o(s)$, as (37) [40]

$$i_2(s) = G_{cl}\, i_{ref} - \frac{v_{PCC}(s)}{Z_o(s)}. \tag{37}$$

TABLE 5. Main Electrical and Control Parameters of the Single-Phase *LCL*-Filtered GCI

Parameter	Value	Parameter	Value
V_{grid}	127 V/60 Hz	L_g; R_g	0.33 mH; 0.1 Ω
P_{LES}; V_{dc}	3 kW; 235 V	L_1; R_1	1.4 mH; 10 mΩ
C_f	22 μF	L_2; R_2	23 μH; 10 mΩ
ζ	0.975	B_r	1.5 Hz
ω_0	377 rad/s	f_{sw};f_{parks}	18 kHz, 90 kHz

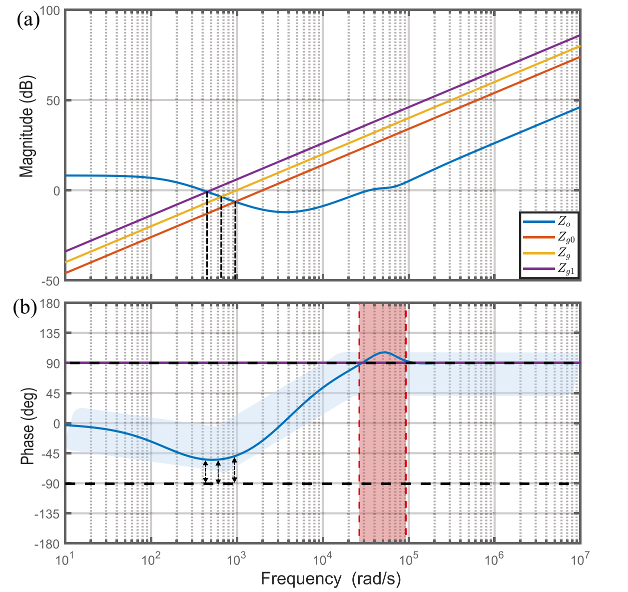

FIGURE 11. Frequency responses of the GCI output impedance under grid impedance variations. (a) Magnitude. (b) Phase.

According to the derivation procedure presented in [39], the inverter output impedance of the GCI is obtained as follows:

$$Z_o = \frac{1 + T_m}{Y_{oc}} \tag{38}$$

$$T_m(s) = G_c(s)\, G_d(s)\, K_{PWM}\, Y_m(s)\, H_i(s). \tag{39}$$

For the system to remain stable, the impedance ratio Z_o/Z_g must satisfy the Nyquist stability criterion. For this condition, the amplitude-phase characteristic curves of the two impedances do not intersect, or the phase margin ϕ_m at the intersection frequency, f_i, must be greater than zero, i.e., expressed in (40) [41], [42]

$$\phi_m = 180^\circ - [\angle Z_g(j2\pi f_i) - \angle Z_o(j2\pi f_i)] > 0. \tag{40}$$

Based on the parameters in Table 5 and the Lanczos differentiator, for example, the Bode diagram of $Z_{out}(s)$ can be obtained in Fig. 11, evaluated under different impedance values, namely 0.5 mH (Z_{g0}), 1 mH (Z_g), and 2 mH (Z_{g1}), aiming at a more comprehensive stability assessment. Considering the 1 mH impedance case, note that the phase margin at the intersection frequency with the grid impedance is approximately 36°, which is lower than 90° and satisfies the stability condition established in [41]. On the other hand, the results consistently demonstrate that the GCI remains stable under impedance variations, including in the region near the Nyquist frequency, confirming the system stability over the entire considered operating range. Conversely, if this angle were negative, the system could become susceptible to oscillatory behavior, potentially leading to overall instability [43]. Moreover, the output impedance exhibits minor deviations from the passivity condition, whose solution to guarantee complete passivity within the context of this work will be investigated and addressed in future studies.

The impact of the digital implementation is analyzed; thus, (8) is converted into the s-domain by replacing z with e^{sT_s} [44]. By comparing the upper limit of the matching band of the Lanczos differentiator, in Fig. 2, with the corresponding converter output impedance considering its implementation, in Fig. 11, it is verified that stability is ensured up to the end of this frequency range. It is observed, however, that the output impedance exhibits minor deviations from the passivity condition. These deviations arise both from modeling the inverter impedance in the s-domain and from the limited matching band of the differentiator. It is worth emphasizing that beyond the end of the matching band, around 3×10^4 rad/s, a maximum plotting error is observed, and the output impedance begins to exhibit small angular deviations on the order of 10° to 15°, locally violating the passivity condition. Nevertheless, the system remains passive over the remaining frequency ranges. To mitigate this limitation, several AD techniques have been proposed to extend the stable frequency region. Further details can be found in [45], which are beyond the scope of this article.

C. DESIGN CONSIDERATIONS FOR THE PROPOSED CVAD STRATEGY

The switching frequency is a key parameter in GCI design, as it affects the *LCL* filter sizing, controller design, and converter losses. Typical values reported in the literature and adopted in commercial converters range from 12 to 24 kHz, with 18 kHz often selected as a practical compromise between waveform quality and acoustic considerations. In the proposed AD approach based on the LF differentiators, the sampling frequency is more critical than the switching frequency. It must be higher than the switching frequency to accurately capture the capacitor voltage ripple and minimize phase distortions in the estimated current. To ensure deterministic timing, a partitioning strategy using an independent PWM peripheral was adopted, generating a 90 kHz interrupt for the differentiator, while the control loop operates at 18 kHz. Although different switching frequencies could be employed with an appropriate redesign of the *LCL* filter and PR controller, the differentiator sampling frequency has a stronger influence on the stability margins of the CVAD implementation. Therefore, 90 kHz was selected as a multiple of both switching and fundamental frequencies. Further details can be found in [46].

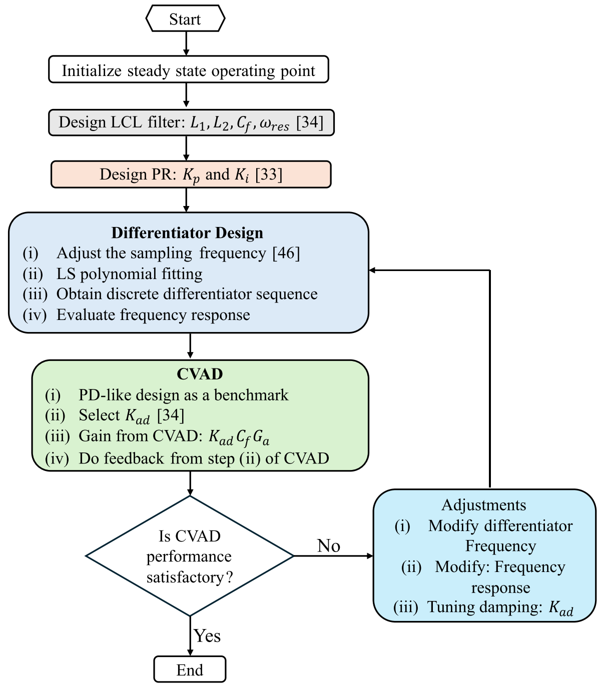

FIGURE 12. Flowchart of the proposed step-by-step design procedure CVAD.

The delay introduced by the sampling and differentiator computation processes manifests itself as an additional phase lag in the control loop, thereby reducing the phase margin and potentially compromising the robustness of the GCI. Moreover, increasing time delay intensifies grid-side current oscillations, especially peak currents excursions, imposing higher stress on the power switches and requiring overcurrent protection strategies [47]. Although adjustments in the switching frequency, *LCL* filter parameters, and PR controller tuning may preserve similar overall system performance after redesign, changes in the sampling frequency directly affect system stability due to the additional phase lag introduced by the differentiator, which reduces the phase margin of the AD loop [48]. Furthermore, differentiator design inherently involves a tradeoff between noise amplification and phase lag, which must be assessed through frequency response analysis [16].

Furthermore, Fig. 12 summarizes a systematic and iterative design procedure for a GCI employing CVAD. Initially, the *LCL* filter is designed by determining the parameters L_1, L_2, and C_f, together with the resulting resonance frequency ω_{res}, which defines the dynamic behavior of the system. Subsequently, the PR controller is designed through the definition of the proportional gain and resonant gain, ensuring accurate reference tracking under sinusoidal operating conditions. Next, the differentiator is synthesized to emulate the continuous-time operator "s." This stage includes defining the differentiator sampling frequency, computing the differentiator coefficients through LS polynomial fitting, and evaluating the differentiator frequency response.

Afterward, the CVAD strategy is implemented. For this purpose, a passive damping structure composed of a resistor connected in series with the capacitor is adopted as the reference for the analyzes. Then, the damping gain, K_{ad}, of the CVAD strategy is defined according to the procedure presented in [34]. The capacitor voltage is measured and multiplied by K_{ad}, the filter capacitance C_f, and the differentiator transfer function (G_a), which emulates the differentiation process. The resulting signal is then feedback to the modulator input in order to provide AD. Finally, the system performance is evaluated to verify whether the CVAD strategy satisfies the desired specifications. If the performance is not satisfactory, an iterative tuning procedure is carried out, including adjustments in the differentiator sampling frequency, differentiator parameters (frequency response), and damping gain. This process is repeated until the desired performance is achieved.

V. EXPERIMENTAL RESULTS

In order to evaluate the effectiveness of the proposed control strategy, experimental validation based on hardware-in-the-loop (HIL) results and experimental prototype, as shown in Fig. 13 has been developed to certify the digital control approach for real applications. It is worth noting that HIL validation has been extensively employed in the literature, as reported in [49]. In the following, further details on the HIL validation and the experimental setup are described.

The prototype parameters are given in Table 5, and the following sections present the experimental validation of the proposed scheme of CVAD. According to Table 5, the K_p and K_i gains of the PR controller are given as 0.0109055 and 0.003368843557, respectively.

A. ANALYSIS CVAD VIA C-HIL

Initially, tests were carried out on a C-HIL platform, in which the power-stage structure is emulated using the HIL402 platform, while the control strategy is implemented on the TMS320F28335 DSC. The interface between the DSC and the HIL402 is established through the Typhoon HIL-DSP-100 interface board, which provides offset and gain adjustments to ensure signal compatibility with the microcontroller input ranges, as illustrated in Fig. 13(a). In this case, the Rigol DS2102 A digital oscilloscope was used to acquire voltage and current waveform signals The system parameters are listed in Table 5.

1) CASE I: CVAD UNDER NOISE INJECTION

In order to assess the robustness and effectiveness of the differentiator and the adopted AD methodology, noise is intentionally injected into the capacitor voltage, which directly affects both the synchronization signal and the CVAD performance. In this case, the Lanczos differentiator was selected due to its superior noise immunity characteristics, which is an essential requirement when dealing with differentiators.

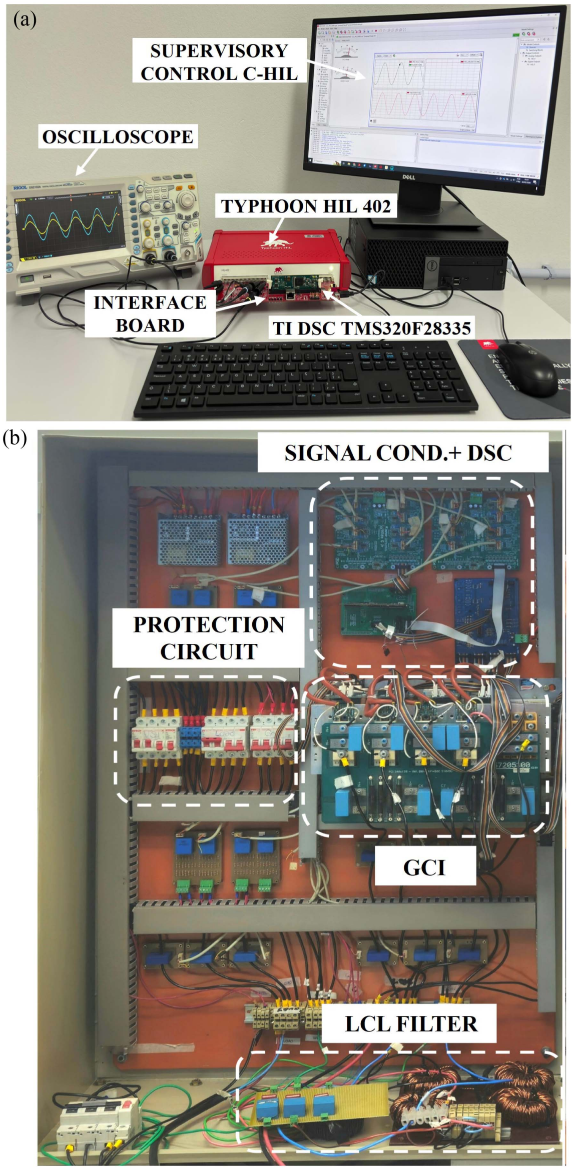

FIGURE 13. Platforms used for result validation. (a) HIL-based validation. (b) Experimental setup of a single-phase LCL–GCI.

In this scenario, the noise injected into the capacitor voltage is generated by a random source with an amplitude corresponding to approximately 2% of the voltage component, which constitutes an excellent performance verification test for the proposed technique, since this situation is highly feasible in industrial environments. Further details are provided in [50]. Moreover, the differentiator was sampled at a frequency of 90 kHz, and system synchronization was achieved based on the measurement of the filter capacitor voltage. To enable a comparative assessment with state-of-the-art methods, the nGI differentiator was selected due to its proven effectiveness in providing high-accuracy derivative estimation, as reported in [11] and [12]. To ensure a fair comparison, the damping gain and current controller parameters were

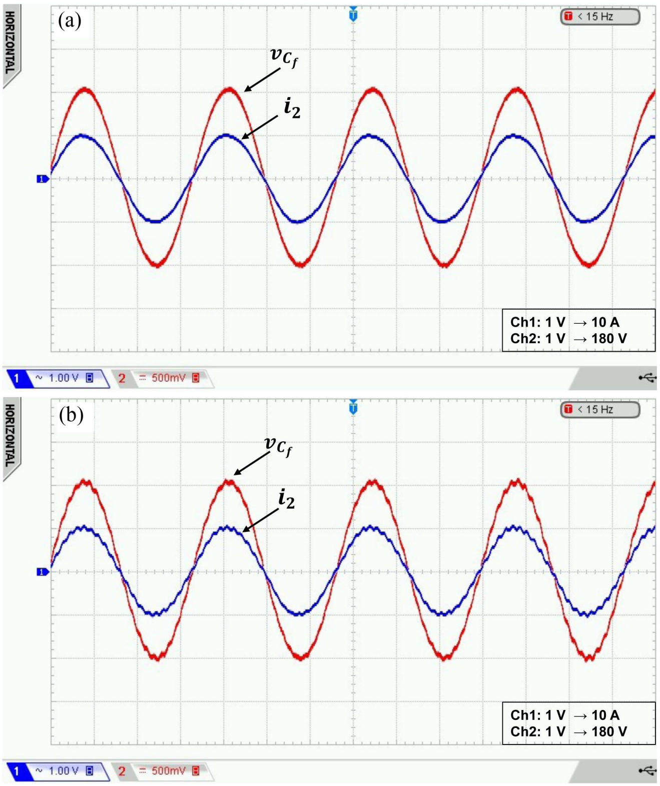

FIGURE 14. C-HIL comparison with the state-of-the-art under noise injection conditions for the CVAD strategy employing. (a) Lanczos differentiator. (b) nGI differentiator [1].

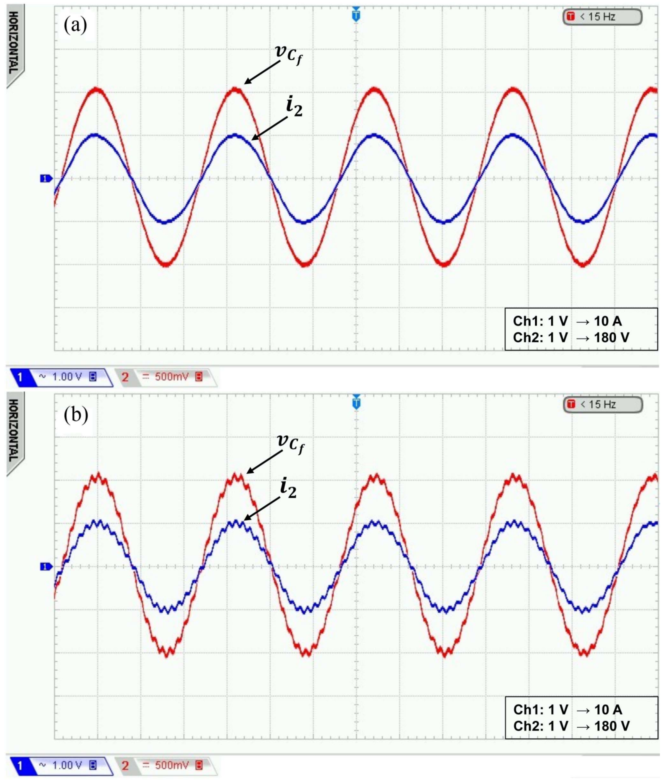

FIGURE 15. C-HIL comparison with the state-of-the-art under noise injection and step frequency variation conditions for the CVAD strategy employing. (a) Lanczos differentiator and (b) nGI differentiator [1].

kept identical across all cases, and the nGI differentiator was discretized at 18 kHz to match the switching frequency, as usually is the case for nGI.

Fig. 14 illustrates the capacitor voltage, $v_{\mathrm{C_f}}$, and the grid-injected current, i_2, in response to an injected disturbance. Fig. 14(a) considers the analysis of the CVAD strategy under noise injection using the Lanczos differentiator. It can be observed that both waveforms exhibit predominantly sinusoidal behavior, indicating stable converter operation. Moreover, the injected current remains well regulated, with controlled amplitude and no high-frequency oscillations, which highlights the effectiveness of the AD strategy in mitigating filter resonances and improving the quality of the current delivered to the grid. It is also observed that the voltage and current remain in phase, indicating a power factor close to unity. Furthermore, the grid current THD_i remained around 2.27%, staying below the recommended 5% limit established by the IEEE std. 519 regulation [51].

Fig. 14(b) presents the analysis of the CVAD strategy under noise injection using the nGI differentiator. In this case, the injected current exhibits high-frequency oscillatory content, indicating that the strategy is not immune to the effects of noise injection, which are reflected in the capacitor voltage. Although stable operation is maintained, such a condition could potentially lead to performance degradation of the CVAD strategy and even affect the synchronization algorithm. Despite these undesirable effects, the proposed technique remains capable of effectively damping the *LCL* filter, maintaining a power factor close to unity. However, the resulting THD_i reached 9.34%, exceeding the limits established by the IEEE standard power quality limits.

Therefore, the results of this scenario confirm that the proposed CVAD strategy ensures system stability, high-quality waveforms without high-frequency oscillations, and effective resonance damping, validating its applicability in the analyzed scenario.

2) CVAD UNDER NOISE INJECTION AND STEP FREQUENCY

Fig. 15 presents a comparative analysis of the CVAD strategy, considering both noise injection into the capacitor voltage and step changes in the source frequency, in which the grid frequency was changed by 2 Hz, i.e., from 60 to 62 Hz. The adopted differentiators are evaluated against the state-of-the-art nGI differentiator in order to demonstrate their effectiveness, while the noise level is maintained identical to that of the previous case. It is worth noting that variations in grid frequency lead to shifts in harmonic components, which, in the worst case, may excite the resonance frequency of the *LCL* filter, potentially resulting in violations of harmonic limits imposed by national grid codes [52].

Fig. 15(a) shows the performance of the CVAD strategy using the Lanczos differentiator under the second scenario. It can be observed that the capacitor voltage and grid current

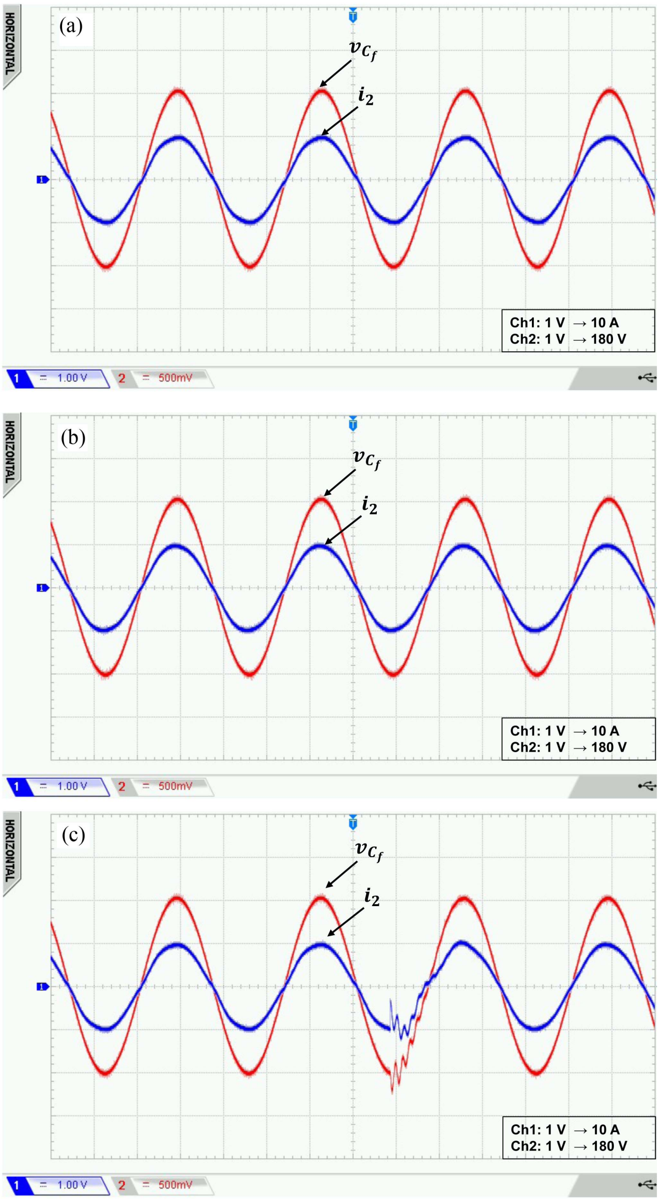

FIGURE 16. **C-HIL analysis of the CVAD strategy under grid-impedance variations. (a) $L_g = 0.5$ mH. (b) $L_g = 1.5$ mH. (c) transition from $L_g = 0.5$ mH to $L_g = 1.5$ mH.**

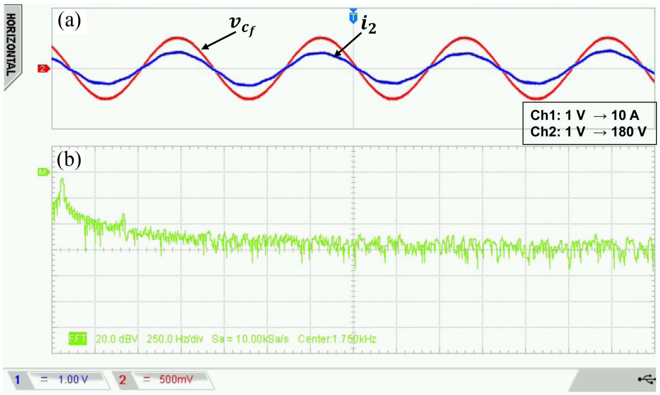

FIGURE 17. **Analysis of the CVAD strategy under the presence of grid harmonics. (a) Result in time-domain. (b) FFT of the current.**

waveforms remain sinusoidal and free of oscillatory components, demonstrating that the strategy is robust even in the presence of noise injection and grid frequency variations. Once again, the voltage and current waveforms remain in phase, ensuring a unity power factor.

On the other hand, the CVAD strategy employing the nGI differentiator is presented in Fig. 15(b). In this case, high-frequency oscillations are more pronounced than in the previous scenario, since the nGI differentiator is susceptible to frequency step variations, as reported in [11]. Despite its low computational burden and proven effectiveness for CVAD under disturbance-free conditions, this differentiator exhibits limited immunity when the capacitor voltage is used for the synchronization algorithm under abrupt frequency variations. Consequently, these results indicate that the CVAD approach based on the Lanczos differentiator represents a feasible and robust alternative to the nGI-based solution.

3) CVAD UNDER VARIATIONS IN GRID IMPEDANCE

Fig. 16 depicts the behavior of the grid-injected current and the capacitor voltage, which approaches the PCC voltage, during the analysis of the CVAD strategy under variations in grid impedance. Fig. 16(a) illustrates the first scenario, considering a strong grid with line inductance $L_g = 0.5$ mH. In this case, the injected current maintains a predominantly sinusoidal waveform, presenting a THDi of approximately 2.76%. In turn, Fig. 16(b) addresses a weak-grid condition, with line inductance $L_g = 1.5$ mH [53]. Even under this condition, the injected current continues to exhibit a sinusoidal waveform, while the THD_i is reduced to approximately 2.23%. Finally, Fig. 16(c) analyzes the impact of a sudden variation in line impedance, corresponding to the transition from $L_g = 0.5$ mH to $L_g = 1.5$ mH. It can be observed that, even under this external disturbance, the GCI remains stably operating, highlighting the robustness of the proposed strategy under both strong-grid and weak-grid conditions.

4) CVAD UNDER THE PRESENCE OF GRID HARMONICS

With the aim of evaluating the disturbance rejection capability of the GCI, the presence of grid harmonics was considered, more specifically a seventh-order harmonic component with an amplitude corresponding to 1% of the fundamental voltage component, in addition to a weak-grid scenario, as shown in Fig. 17. Under these conditions, the injected current, in Fig. 17(a), remains predominantly sinusoidal, although slight distortions are observed, as evidenced by the increase in THD_i to approximately 4.16%, which is higher than that observed in the previous scenario. In turn, Fig. 17(b) shows the harmonic spectrum of the injected current obtained from the FFT analysis under this scenario. It can be observed that the harmonic components are predominantly concentrated at low amplitudes, indicating that the proposed CVAD strategy

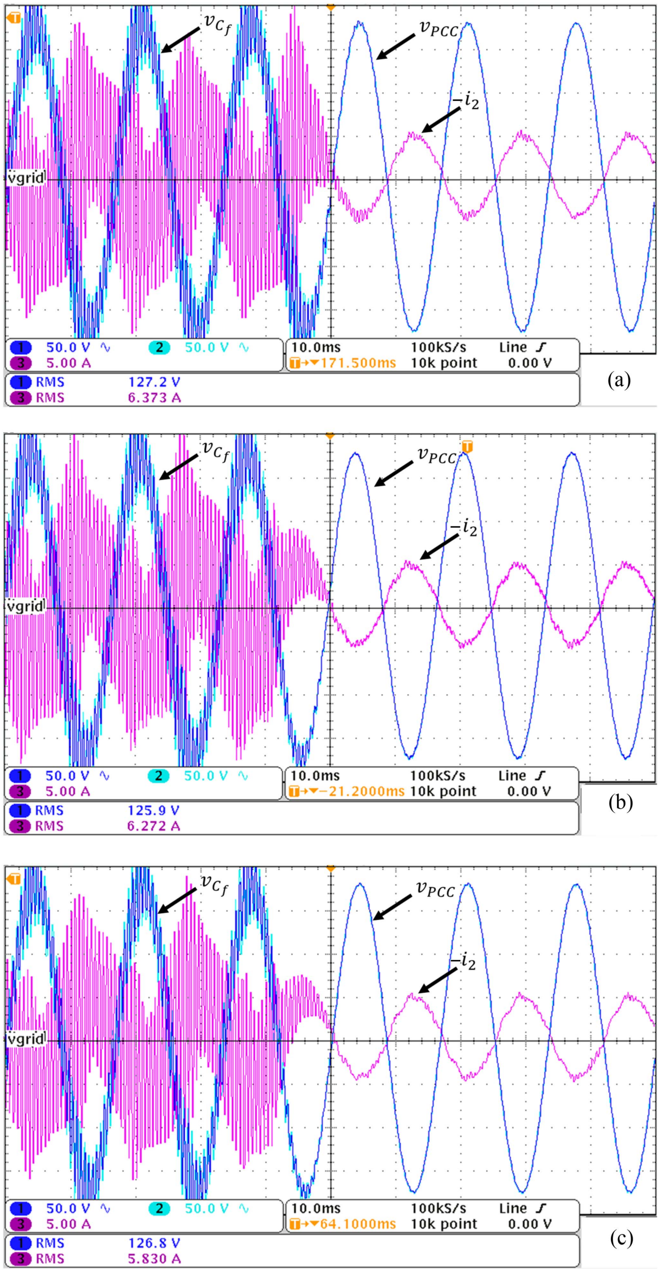

FIGURE 18. **Experimental steady-state response of the inverter with AD disabled and enabled using. (a) Lanczos, (b) SL1, and (c) SL2.**

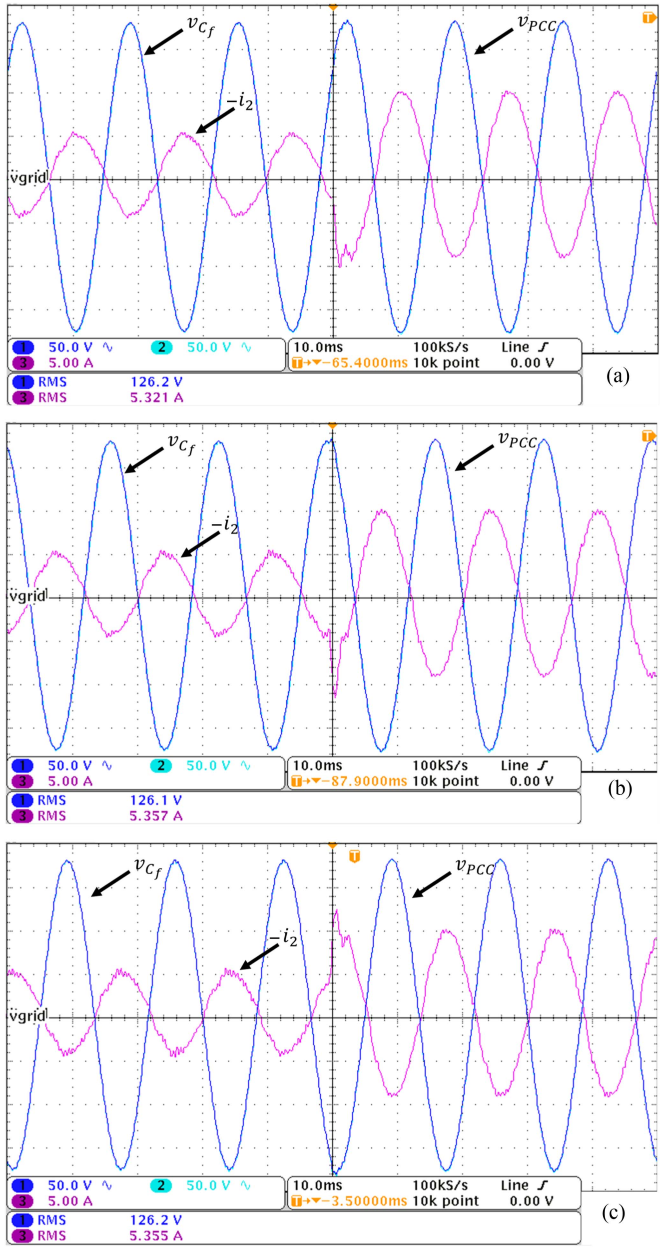

FIGURE 19. **Experimental transient response to a 50% step increase in the injected-current reference using. (a) Lanczos, (b) SL1, and (c) SL2.**

is capable of attenuating the propagation of harmonic disturbances to the injected current. In addition, no significant resonance peaks are observed around the *LCL* filter resonance region, demonstrating the effectiveness of the AD method in maintaining system stability even under distorted grid conditions.

B. ANALYSIS CVAD VIA EXPERIMENTAL SETUP

The experimental setup of the single-phase inverter uses SEMIKRON SEMiX 403GB128Ds IGBT modules with Skyper 32PRO gate drivers. A 3 kVA GCI with an *LCL* filter was adopted for experiments, and the DC bus of the inverter is fed with 235 V_{dc} by a bidirectional DC voltage source from ITECH (model IT6012C-800-50). The prototype also uses a bidirectional grid emulator (model TC.ACS.30.528.4WR, from Regatron), providing a phase voltage of 127 V_{rms} at 60 Hz. Line impedances, $Z_{L1} = 0.18 + j0.188\ \Omega$, connecting the grid to the PCC of the prototype, were implemented via cables. In addition, analog conditioning circuits based on LEM LV-25P and LA-55P sensors are employed to measure voltage and current throughout the setup.

The TMS320F28379D DSC from Texas Instruments embeds the GCI's control algorithm using code composer studio, considering sampling and switching frequencies of 18 kHz. The DPO3000 oscilloscope from Tektronix is used to acquire voltage and current waveforms. It is worth noting that the sampling frequency was adjusted to 90 kHz, ensuring an integer multiple of both the switching and fundamental frequencies, thereby guaranteeing an exact sample count. Additional details are discussed in [8].

1) CASE I: STEADY-STATE PERFORMANCE VALIDATION

The first set of experiments was conducted to assess the performance of CVAD using Lanczos, SL1, and SL2 differentiators in an ideal grid. Initially, with CVAD disabled, significant oscillations were observed in the grid-current waveform, as shown in Fig. 18. However, when AD was enabled, these high-frequency oscillations were no longer visible in the grid-current waveform. It is important to note that, with AD disabled, the current control scheme reverts to a single-loop grid-current control, which remains stable only above $f_s/6$ [54]. Consequently, although the grid current is stable, the system fails to effectively mitigate resonance.

Comparing the performance of the AD strategy with the activation of the three proposed differentiators qualitatively, it is observed that the Lanczos differentiator produces a waveform with a shape closer to a sine wave. However, it also exhibits pronounced oscillations at the peak of the waveform, which are associated with the effects originating from the capacitor voltage and system noise, including switching sources, commutation processes, and interactions with the grid emulation source. On the other hand, the SL2 differentiator results in a more distorted waveform but with reduced oscillations, while the SL1 differentiator shows performance that is intermediate between the two. It is important to emphasize that the voltage and current waveforms exhibit a 180° phase shift due to the signal acquisition process. In the analyzed cases, a power factor close to unity and a current THD of approximately 3.5% were achieved, remaining below the 5% limit established by the IEEE standard.

2) CASE II: STEP-UP IN THE CURRENT REFERENCE

The GCI with an *LCL* filter is subject to abrupt changes in reference current during operation. In this context, the second scenario examines a step change in the current injected into the grid and evaluates the dynamic response of the control system. This is crucial for determining how quickly the system can reach the desired reference current and how it maintains stability under transient conditions. The dynamic response of the current control scheme is assessed based on the transient response to a 50% change in the current reference value, as demonstrated in [55], where the output power is shifted from half load to full load.

According to Fig. 19, the results show that the injected current can quickly track the reference within 5 ms, with minimal settling time and an overshoot around 10%–15%, demonstrating the excellent dynamic response of the proposed method. In addition, the SL1 differentiator is capable of tracking the reference command change with a good response time compared to the other two differentiators, although it exhibits the highest overshoot.

Furthermore, the CVAD with Lanczos and SL2 shows minimal oscillation during the reference step, while the SL2 differentiator has a higher overshoot but demonstrates a rapid dynamic response.

VI. CONCLUSION

This article introduced an active *LCL*-resonance damping method for GCIs, utilizing capacitor voltage feedback and Lanczos, SL1 and SL2 differentiators. The proposed method successfully achieved AD by estimating the capacitor current through the derivative of the capacitor voltage using the Lanczos, SL1 and SL2 differentiator, eliminating the need for an additional current sensor. The performance of all differentiators from the LF was evaluated, as well as their practical application, thereby expanding the possibilities of using these differentiators in CVAD strategies, since they had not been employed in this type of application.

A key consideration in implementing the differentiator is balancing the tradeoff among noise rejection capability, reduced phase delay and good performance under dynamic variations. The results obtained through C-HIL demonstrate that the Lanczos differentiator exhibits excellent performance even in the presence of noise in the capacitor voltage and under variations in the source frequency, thus representing a promising alternative to the nGI differentiator. Experimental results demonstrated satisfactory performance, with Lanczos, SL1 and SL2 differentiators showed similar dynamic response and waveforms. From an implementation standpoint, the system exhibited susceptibility to noise from switching power supply, which was mitigated by integrating filtering capacitors directly onto the DSC board. The proposed methodology is noteworthy for achieving AD without additional sensors. By utilizing the capacitor voltage for simultaneous AD and PLL operation, the proposed approach simplifies the control structure while enhancing system stability and reducing sensor count. Future work will address the integration of additional functionalities into the control framework, including active filtering, as well as the enhancement of wideband dissipativity under weak grid conditions.

APPENDIX I

This Appendix presents the steps to determine the coefficients of the Lanczos differentiators. The content of this Appendix is based on the books [19], [56], [57], [58], [59].

A. LANCZOS DIFFERENTIATOR

For each point, take that point together with its two neighboring points, one to the left and one to the right, and combine them. This operation produces a fourth-difference sequence of points, which smooths the data. In the end, five consecutive points are obtained, which are assumed to lie on a parabolic curve described by

$$y = a + bx + cx^2 \tag{41}$$

where a, b, c are the coefficients to be adjusted to be used in the Lanczos differentiators. Since three parameters cannot be adjusted to five data points, the principle of LS is used, given by

$$P = \sum_{k=-2}^{2} (y - y_k)^2 \tag{42}$$

by combining (41) and (42), it results in

$$P = \sum_{k=-2}^{2} (a + bx + cx^2 - y_k)^2 \tag{43}$$

$$\begin{aligned} P = (a - 2b + 4c - y_{-2})^2 + (a - b + c - y_{-1})^2 \\ + (a - y_0)^2 + (a + b + c - y_1)^2 \\ + (a + 2b + 4c - y_2)^2. \end{aligned} \tag{44}$$

By computing the partial derivative with respect to b, it is obtained

$$\frac{\partial}{\partial b}\left[f(a,b,c)\right]^2 = 2f(a,b,c)\frac{\partial f(a,b,c)}{\partial b} \tag{45}$$

$$\begin{aligned} \frac{\partial P}{\partial b} &= 2(a - 2b + 4c - y_{-2})(-2) \\ &+ 2(a - b + c - y_{-1})(-1) + 0 \\ &+ 2(a + b + c - y_1)(1) \\ &+ 2(a + 2b + 4c - y_2)(2) \end{aligned} \tag{46}$$

which results in

$$\frac{\partial P}{\partial b} = 20b + 2(2y_{-2} + y_{-1} - y_1 - 2y_2). \tag{47}$$

By making the partial derivative equal to zero and isolating b, it results in

$$\frac{\partial P}{\partial b} = 0 \tag{48}$$

$$b = \frac{1}{5}y_2 + \frac{1}{10}y_1 + 0y_0 - \frac{1}{10}y_{-1} - \frac{1}{5}y_{-2}. \tag{49}$$

This results in the following set of coefficients:

$$h = \left\{\frac{1}{5}; \frac{1}{10}; 0; -\frac{1}{10}; -\frac{1}{5}\right\}. \tag{50}$$

B. SL1 DIFFERENTIATOR

The ideal differentiator in s-domain is given by

$$H(s) = s. \tag{51}$$

And its function for frequency response is given by

$$H(s) = j\omega. \tag{52}$$

For an FIR filter with coefficients that have odd symmetry, it is possible to write

$$h_{-k} = -h_k. \tag{53}$$

The output sequence of the FIR filter is given by

$$y_n = \sum_{k=-N}^{N} h_k u_{n-k} \tag{54}$$

where h_k are the coefficients. The frequency response function is given by

$$H(\omega) = \sum_{k=-N}^{N} h_k e^{-j\omega k}. \tag{55}$$

For negative and positive values of k, we have, respectively

$$h_k e^{-j\omega k} = h_{-k} e^{j\omega k} \tag{56}$$

which can be written as

$$H(\omega) = \sum_{k=-N}^{N} \left(h_k e^{-j\omega k} + h_{-k} e^{j\omega k}\right) \tag{57}$$

which is also equal to

$$H(\omega) = \sum_{k=-N}^{N} h_k \left(e^{-j\omega k} - e^{j\omega k}\right). \tag{58}$$

Giving the Euler's identity, expressed as

$$\sin(\omega k) = \frac{e^{j\omega k} - e^{-j\omega k}}{2j}. \tag{59}$$

Then, we have

$$H(\omega) = \sum_{k=-N}^{N} -h_k[2j\sin(\omega k)]. \tag{60}$$

The Taylor series for $\sin(x)$ is given by

$$\sin(x) = x - \frac{x^3}{3!} + \frac{x^5}{5!} - \cdots. \tag{61}$$

So

$$\sin(k\omega) \approx k\omega - \frac{(k\omega)^3}{6}. \tag{62}$$

Then,

$$H(\omega) = \sum_{k=-N}^{N} -h_k \left[2j\left(k\omega - \frac{(k\omega)^3}{6}\right)\right]. \tag{63}$$

Arranging it, it leads to

$$\frac{H(\omega)}{j} = 2\omega \sum_{k=-N}^{N} h_k k - \frac{2\omega^3}{6}\sum_{k=-N}^{N} h_k k^3. \tag{64}$$

To make this filter close to an ideal differentiator, the first term of the right side of the equation must be equal to 1 and the second term must be equal to zero, ensuring noise filtering

$$\sum_{k=-N}^{N} h_k k = 1 \tag{65}$$

$$\sum_{k=-N}^{N} h_k k^3 = 0. \tag{66}$$

For $N = 2$

$$\sum_{k=-2}^{2} h_k k = h_{-2}(-2) + h_{-1}(-1) + 0 + h_1(1) + h_2(2) \tag{67}$$

$$\sum_{k=-N}^{N} h_k k^3 = h_{-2}(-8) + h_{-1}(-1) + 0 + h_1(1) + h_2(8). \tag{68}$$

Then, the following system of equations can be written:

$$\begin{cases} -2h_{-2} - h_{-1} + h_1 + 2h_2 = 1 \\ -8h_{-2} - h_{-1} + h_1 + 8h_2 = 0. \end{cases} \tag{69}$$

Since $h_{-2} = h_2$ and $h_{-2} = -h_2$, the system results in

$$\begin{cases} 4h_2 + 2h_1 = 1 \\ 16h_2 + 2h_1 = 0. \end{cases} \tag{70}$$

Subtracting the first equation in the second, it results in

$$-12h_2 = 1. \tag{71}$$

Therefore

$$h_2 = -\frac{1}{12}. \tag{72}$$

In addition, using it in the system, it results in

$$h_1 = \frac{8}{12}. \tag{73}$$

Using these results, with (53), in (54), we get the super Lanczos differentiator, which is given by

$$y_n = -\frac{1}{12}u_{n-2} + \frac{8}{12}u_{n-1} + 0u_n - \frac{8}{12}u_{n+1} + \frac{1}{12}u_{n+2}. \tag{74}$$

Therefore, the coefficients are

$$h = \left\{-\frac{1}{12}; \frac{8}{12}; 0; -\frac{8}{12}; \frac{1}{12}\right\}. \tag{75}$$

C. SL2 DIFFERENTIATOR

For the SL2 differentiator, the procedure is similar to the Lanczos, but instead of using a parabolic function, a cubic function is used, which is given by

$$y = a + bx + cx^2 + dx^3. \tag{76}$$

Besides that, one should use $N = 3$, reaching the expression of

$$P = \sum_{k=-3}^{3} (a + bx + cx^2 + dx^3 - y_k)^2 \tag{77}$$

$$\begin{aligned} P = {} & (a - 3b + 9c - 27d - y_{-3})^2 \\ & + (a - 2b + 4c - 8d - y_{-2})^2 \\ & + (a - b + c - d - y_{-1})^2 \\ & + (a - y_0)^2 + (a + b + c + d - y_1)^2 \\ & (a + 2b + 4c + 8d - y_2)^2 \\ & + (a + 3b + 9c + 27d - y_3)^2. \end{aligned} \tag{78}$$

Similar the Lanczos differentiators, only the coefficients b and d results partial derivatives that can be arranged into a system of equations

$$\begin{aligned} \frac{\partial P}{\partial b} = {} & -6\,(a - 3b + 9c - 27d - y_{-3}) \\ & -4\,(a - 2b + 4c - 8d - y_{-2}) \\ & -2\,(a - b + c - d - y_{-1}) \\ & +2\,(a + b + c + d - y_1) \\ & +4\,(a + 2b + 4c + 8d - y_2) \\ & +6\,(a + 3b + 9c + 27d - y_3) = 0 \end{aligned} \tag{79}$$

$$\begin{aligned} \frac{\partial P}{\partial d} = {} & -54\,(a - 3b + 9c - 27d - y_{-3}) \\ & -16\,(a - 2b + 4c - 8d - y_{-2}) \\ & -2\,(a - b + c - d - y_{-1}) \\ & +2\,(a + b + c + d - y_1) \\ & +16\,(a + 2b + 4c + 8d - y_2) \\ & +54\,(a + 3b + 9c + 27d - y_3) = 0. \end{aligned} \tag{80}$$

With the two partial derivatives, the following system of equations is created:

$$\begin{cases} 28b + 196d = -3y_{-3} - 2y_{-2} - y_{-1} + 0y_0 \\ \qquad\qquad + y_1 + 2y_2 + 3y_3 \\ 196b + 1588d = -27y_{-3} - 8y_{-2} - y_{-1} + 0y_0 \\ \qquad\qquad + y_1 + 8y_2 + 27y_3. \end{cases} \tag{81}$$

Defining two variables as in

$$S_1 = \sum_{k=-3}^{3} k\, y_k \tag{82}$$

$$S_2 = \sum_{k=-3}^{3} k^3 y_k. \tag{83}$$

Then, we can write

$$\begin{cases} 28b + 196d = S_1 \\ 196b + 1588d = S_2. \end{cases} \tag{84}$$

Solving this system, it results in

$$d = \frac{S_2 - 7S_1}{216} \tag{85}$$

$$b = \frac{397}{1512}S_1 - \frac{49}{1512}S_2. \tag{86}$$

Using now the definition of (82) and (83), it results in

$$b = \frac{397}{1512}\left(\sum_{k=-3}^{3} ky_k\right) - \frac{49}{1512}\left(\sum_{k=-3}^{3} k^3 y_k\right). \tag{87}$$

Now, moving the constants inside the sums

$$b = \sum_{k=-3}^{3}\left(\frac{397}{1512}ky_k\right) - \sum_{k=-3}^{3}\left(\frac{49}{1512}k^3 y_k\right). \tag{88}$$

By combining into a single sum, it results in

$$b = \sum_{k=-3}^{3}\left[\left(\frac{397}{1512}ky_k\right) - \left(\frac{49}{1512}k^3 y_k\right)\right]. \tag{89}$$

Factoring and arranging it, it results in

$$b = \sum_{k=-3}^{3}\left(\frac{397k - 49k^3}{1512}\right)y_k. \tag{90}$$

From (90) and (54), we observe that the term inside the parentheses corresponds to the expression used to compute the filter coefficients, valid for the SL2 differentiator. Therefore, the coefficients of the SL2 are determined by the following equation, where k varies from -3 to 3

$$h_k = \frac{397k - 49k^3}{1512} \tag{91}$$

$$\begin{aligned} h_{-3} &= \frac{22}{252} \\ h_{-2} &= -\frac{67}{252} \\ h_{-1} &= -\frac{58}{252} \\ h_0 &= 0 \\ h_1 &= \frac{58}{252} \\ h_2 &= \frac{67}{252} \\ h_3 &= -\frac{22}{252}. \end{aligned} \tag{92}$$

Using again the property $h_{-k} = -h_k$, the coefficients of the SL2 coefficients are given by

$$h = \left\{-\frac{22}{252}; \frac{67}{252}; \frac{58}{252}; 0; -\frac{58}{252}; -\frac{67}{252}; \frac{22}{252}\right\}. \tag{93}$$

REFERENCES

[1] Z. Xin, P. C. Loh, X. Wang, F. Blaabjerg, and Y. Tang, "Highly accurate derivatives for LCL-filtered grid converter with capacitor voltage active damping," *IEEE Trans. Power Electron.*, vol. 31, no. 5, pp. 3612–3625, May 2016.

[2] D. Pan, X. Ruan, and X. Wang, "Direct realization of digital differentiators in discrete domain for active damping of LCL-type grid-connected inverter," *IEEE Trans. Power Electron.*, vol. 33, no. 10, pp. 8461–8473, Oct. 2018.

[3] R. Huang, X. Quan, Z. Wu, M. Hu, Q. Hu, and Z. Wang, "A novel reduced-order generalized differentiator with zero-phase lag and improved noise attenuation," *IEEE Trans. Power Electron.*, vol. 38, no. 2, pp. 1406–1411, Feb. 2023.

[4] Z. Xin, X. Wang, P. C. Loh, and F. Blaabjerg, "Realization of digital differentiator using generalized integrator for power converters," *IEEE Trans. Power Electron.*, vol. 30, no. 12, pp. 6520–6523, Dec. 2015.

[5] R. Huang et al., "An equivalent linearized discrete-time realization of optimal control based tracking differentiator," *IEEE Trans. Ind. Electron.*, vol. 71, no. 2, pp. 1832–1841, Feb. 2024.

[6] J. Dannehl, F. W. Fuchs, S. Hansen, and P. B. Thøgersen, "Investigation of active damping approaches for PI-based current control of grid-connected pulse width modulation converters with LCL filters," *IEEE Trans. Ind. Appl.*, vol. 46, no. 4, pp. 1509–1517, Jul./Aug. 2010.

[7] J. Du et al., "Tracking differentiator based approximate zero-impedance control for three-phase grid-forming inverter," *IEEE Open J. Power Electron.*, vol. 6, pp. 1583–1594, 2025.

[8] L. Harnefors, A. G. Yepes, A. Vidal, and J. Doval-Gandoy, "Passivity-based controller design of grid-connected VSCs for prevention of electrical resonance instability," *IEEE Trans. Ind. Electron.*, vol. 62, no. 2, pp. 702–710, Feb. 2015.

[9] Y. Chen et al., "Optimized design method for grid-current-feedback active damping to improve dynamic characteristic of LCL-type grid-connected inverter," *Int. J. Elect. Power Energy Syst.*, vol. 100, pp. 19–28, 2018. [Online]. Available: https://www.sciencedirect.com/science/article/pii/S0142061516328794

[10] R. Peña-Alzola, M. Liserre, F. Blaabjerg, R. Sebastián, J. Dannehl, and F. W. Fuchs, "Systematic design of the lead-lag network method for active damping in LCL-filter based three phase converters," *IEEE Trans. Ind. Informat.*, vol. 10, no. 1, pp. 43–52, Feb. 2014.

[11] J. de Arimatéia Olímpio Filho et al., "Active damping of LCL resonance in grid-connected inverters through capacitor–voltage feedback and the Parks–McClellan algorithm," *IEEE Trans. Emerg. Sel. Topics Power Electron.*, vol. 13, no. 3, pp. 3397–3410, Jun. 2025.

[12] S. Ke and Y. Li, "An improved active damping method for enhancing robustness of LCL-type, grid-tied inverters under weak grid conditions," *Sensors*, vol. 23, no. 19, 2023, Art. no. 8203. [Online]. Available: https://www.mdpi.com/1424-8220/23/19/8203

[13] M. Li, Y. Ren, H. Xiao, C. Niu, and M. Cheng, "An equivalent differential method for active damping of LCL type grid-connected inverters with grid-side inductor voltage feedback," *IEEE Trans. Power Electron.*, vol. 38, no. 6, pp. 7009–7021, Jun. 2023.

[14] J. Samanes, A. Urtasun, E. Gubia, and A. Petri, "Robust multisampled capacitor voltage active damping for grid-connected power converters," *Int. J. Elect. Power Energy Syst.*, vol. 105, pp. 741–752, 2019. [Online]. Available: https://www.sciencedirect.com/science/article/pii/S0142061518315825

[15] H. Zhang, G. Xiao, X. Yu, and Y. Xie, "On convergence performance of discrete-time optimal control based tracking differentiator," *IEEE Trans. Ind. Electron.*, vol. 68, no. 4, pp. 3359–3369, Apr. 2021.

[16] J. Zeng, Y. Yang, Y. Xiao, and Z. Ni, "Enhancing stability and harmonic rejection ability of LCL-type grid-connected inverter with high-gain tracking differentiator," *Electric Power Syst. Res.*, vol. 253, 2026, Art. no. 112565. [Online]. Available: https://www.sciencedirect.com/science/article/pii/S0378779625011526

[17] P. F. Ribeiro, C. A. Duque, P. M. Silveira, and A. S. Cerqueira, *Power Systems Signal Processing for Smart Grids*. Hoboken, NJ, USA: Wiley, 2013.

[18] P. Holoborodko, "Smooth noise robust differentiators," 2008. Accessed: Jan. 5, 2026. [Online]. Available: http://www.holoborodko.com/pavel/numerical-methods/numerical-derivative/smooth-low-noise-differentiators/

[19] R. G. Lyon, *Understanding Digital Signal Processing*, 3rd ed. London, U.K.: Pearson, 2011.
[20] R. A. Becerra-Garcıá, R. Garcıá-Bermúdez, and G. Joya, "Differentiation of saccadic eye movement signals," *Sensors*, vol. 21, no. 15, 2021, Art. no. 5021. [Online]. Available: https://www.mdpi.com/1424-8220/21/15/5021
[21] B. M. Schettino, C. A. Duque, P. M. Silveira, P. F. Ribeiro, and A. S. Cerqueira, "A new method of current-transformer saturation detection in the presence of noise," *IEEE Trans. Power Del.*, vol. 29, no. 4, pp. 1760–1767, Aug. 2014.
[22] T. D. C. Busarello, "Contributions to discrete-time sliding mode observers for permanent magnet synchronous motor drive systems," in *Proc. 4th Glob. Power, Energy Commun. Conf.*, 2022, pp. 162–167.
[23] T. D. Curi Busarello, "Enhanced discrete-time differentiators for state observers of sensorless permanent magnetic synchronous motor drives," in *Proc. IEEE 8th Southern Power Electron. Conf. 17th Braz. Power Electron. Conf.*, 2023, pp. 1–8.
[24] The MathWorks Inc., "Practical introduction to digital filtering," Online, 2024. Accessed: Apr. 20, 2024. [Online]. Available: https://la.mathworks.com/help/signal/ug/practical-introduction-to-digital-filtering.html
[25] N. S. Figueiredo, L. H. C. Ferreira, and O. O. Dutra, "An approach to Savitzky–Golay differentiators," *Circuits, Syst., Signal Process.*, vol. 38, no. 9, pp. 4369–4379, Sep. 2019.
[26] R. G. Lyons, Ed., *Streamlining Digital Signal Processing: A Tricks of the Trade Guidebook*, 2nd ed. Hoboken, NJ, USA: Wiley-IEEE Press, 2012.
[27] A. Akhavan, S. Golestan, J. C. Vasquez, J. M. Guerrero, and C. Xie, "Stability enhancement of inverters in grid-connected microgrids using FIR filter," *IEEE J. Emerg. Sel. Topics Ind. Electron.*, vol. 2, no. 2, pp. 122–131, Apr. 2021.
[28] R. W. Schafer, "What is a Savitzky-Golay filter? [lecture notes]," *IEEE Signal Process. Mag.*, vol. 28, no. 4, pp. 111–117, Jul. 2011.
[29] X. Yang, "Design of digital differentiators," Ph.D thesis, Dept. Elect. Electron. Eng., Univ. College Cork, Cork, Ireland, 2014.
[30] L. L. Rodrigues, O. C. Velasquez, L. F. N. Lourenço, O. A. C. Vilcanqui, M. B. C. Salles, and A. J. S. Filho, "Filtered repetitive MPC applied to DFIG grid side converter frequency support in microgrids during island operation," *IEEE Access*, vol. 11, pp. 80835–80853, 2023.
[31] J. K. Nielsen, M. G. Christensen, and J. B. Boldt, "An analysis of traditional noise power spectral density estimators based on the Gaussian stochastic volatility model," *IEEE/ACM Trans. Audio, Speech, Lang. Process.*, vol. 31, pp. 2299–2313, 2023.
[32] R. Zhang, S. Chi, X. Xing, C. Zhang, and F. Blaabjerg, "Passivity-based zero-sequence LC resonance suppression method for parallel inverters system with modified LCL filter," *IEEE Trans. Power Electron.*, vol. 41, no. 2, pp. 2618–2628, Feb. 2026.
[33] T. D. Curi Busarello, J. F. Guerreiro, M. G. Simões, and J. A. Pomilio, "Hardware-in-the-loop experimental setup of a LCL-filtered grid-connected inverter with digital proportional-resonant current controller," in *Proc. IEEE 22nd Workshop Control Modelling Power Electron.*, 2021, pp. 1–8.
[34] X. Ruan, X. Wang, D. Pan, D. Yang, W. Li, and C. Bao, *Control Techniques for LCL-Type Grid-Connected Inverters*. Singapore: Springer, 2018.
[35] K. Wang, C. Gao, J. Xu, S. Qin, and C. Qi, "A review of small-signal stability analysis methods of large-scale power electronic systems," *CSEE J. Power Energy Syst.*, doi: 10.17775/CSEEJPES.2025.00900.
[36] R. Strunk, P. Sourkounis, L. Ostuwar, and A. Mertens, "Impedance-based stability analysis of droop-controlled inverters considering the inner control, the interlock time and RHP poles," *IEEE Trans. Emerg. Sel. Topics Power Electron.*, vol. 14, no. 2, pp. 1790–1803, Apr. 2026.
[37] R. Ali and T. O'Donnell, "Analysis and mitigation of harmonic resonances in multi-parallel grid-connected inverters: A review," *Energies*, vol. 15, no. 15, 2022, Art. no. 5438.
[38] A. Akhavan, H. R. Mohammadi, J. C. Vasquez, and J. M. Guerrero, "Passivity-based design of plug-and-play current-controlled grid-connected inverters," *IEEE Trans. Power Electron.*, vol. 35, no. 2, pp. 2135–2150, Feb. 2020.
[39] Z. Zhao, H. Yi, Y. Li, X. Jiang, F. Wang, and F. Zhuo, "Passivity enhancement for LCL-filtered grid-connected inverter based on capacitor voltage proportional-derivative feedback active damping," in *Proc. IEEE 12th Energy Convers. Congr. Expo. - Asia*, 2021, pp. 1354–1359.
[40] C. Wang et al., "Passivity-oriented impedance shaping for LCL-filtered grid-connected inverters," *IEEE Trans. Ind. Electron.*, vol. 70, no. 9, pp. 9078–9090, Sep. 2023.
[41] D. Yang, X. Ruan, and H. Wu, "Impedance shaping of the grid-connected inverter with LCL filter to improve its adaptability to the weak grid condition," *IEEE Trans. Power Electron.*, vol. 29, no. 11, pp. 5795–5805, Nov. 2014.
[42] Y. Han, M. Yang, P. Yang, L. Xu, and F. Blaabjerg, "Passivity-based stability analysis of parallel single-phase inverters with hybrid reference frame control considering PLL effect," *Int. J. Elect. Power Energy Syst.*, vol. 135, 2022, Art. no. 107473.
[43] M. Amin, C. Zhang, A. Rygg, M. Molinas, E. Unamuno, and M. Belkhayat, *Nyquist Stability Criterion and Its Application to Power Electronics Systems*. Hoboken, NJ, USA: Wiley, 2019, pp. 1–22.
[44] C. Li, C. Xie, G. Ma, C. Peng, and J. Zou, "Passivity and injection current quality enhancement for single inverter-side current feedback LCL-type grid-following inverters," *IEEE Trans. Emerg. Sel. Topics Power Electron.*, vol. 13, no. 2, pp. 2500–2511, Apr. 2025.
[45] Z. Yang et al., "Wideband dissipativity enhancement for grid-following VSC utilizing capacitor voltage feedforward," *IEEE Trans. Emerg. Sel. Topics Power Electron.*, vol. 11, no. 3, pp. 3138–3151, Jun. 2023.
[46] J. d. A. Olímpio Filho et al., "Feasibility implementation analysis of the Parks-McClellan algorithm in capacitor voltage active damping," *Eletrônica de Potência*, vol. 31, May 2026, Art. no. e202620.
[47] C. Liao, Z. Liu, H. Wang, and F. Gao, "Small-signal model-based stability analysis for single-phase cascaded h-bridge Statcom considering time delay," *Int. J. Elect. Power Energy Syst.*, vol. 157, 2024, Art. no. 109880.
[48] H. Ge, G. Yuan, and L. Zeng, "Parameter design method for active damping of inverter with LC filter," in *Proc. IEEE 7th Int. Elect. Energy Conf.*, 2024, pp. 1–6.
[49] N. Baschera, M. D. Benedetto, A. Lidozzi, L. Solero, and P. J. Grbović, "Decoupling current ripple in PHIL PMSM emulation using LCL filter: A fundamental frequency analysis," *IEEE Open J. Power Electron.*, vol. 6, pp. 401–415, 2025.
[50] Typhoon HIL Inc., *Random Source—Typhoon HIL Softw. Manual*, Typhoon HIL Inc., Somerville, MA, USA, Documentation HIL do Typhoon—version 2025.04, Apr. 2025.
[51] *IEEE Standard for Harmonic Control in Electric Power Systems*, IEEE Std 519-2022, 2022, pp. 1–31.
[52] R. Meyer and A. Mertens, "Design of LCL filters in consideration of parameter variations for grid-connected converters," in *Proc. IEEE Energy Convers. Congr. Expo.*, 2012, pp. 557–564.
[53] J. Lyu, Y. Yan, F. Wu, Z. Sun, A. Farooq, and W. Xu, "Parameter co-design of active damping loop and grid current controller for a 3-phase LCL-filtered grid-connected inverter," *Int. J. Elect. Power Energy Syst.*, 2021, vol. 133, Art. no. 107203.
[54] Z. Xin, X. Wang, P. C. Loh, and F. Blaabjerg, "Grid-current-feedback control for LCL-filtered grid converters with enhanced stability," *IEEE Trans. Power Electron.*, vol. 32, no. 4, pp. 3216–3228, Apr. 2017.
[55] Z. Xin, P. Mattavelli, W. Yao, Y. Yang, F. Blaabjerg, and P. C. Loh, "Mitigation of grid-current distortion for LCL-filtered voltage-source inverter with inverter-current feedback control," *IEEE Trans. Power Electron.*, vol. 33, no. 7, pp. 6248–6261, Jul. 2018.
[56] C. Lanczos, *Applied Analysis*. Englewood Cliffs, NJ, USA: Prentice-Hall, 1956.
[57] R. Hamming, *Digital Filters* (Dover Civil and Mechanical Engineering). New York, NY, USA: Dover, 2013.
[58] A. Jeffrey, *Advanced Engineering Mathematics*. San Diego, CA, USA: Academic, 2001.
[59] R. Hamming, *Numerical Methods for Scientists and Engineers* (International Series in Pure and Applied Mathematics). New York, NY, USA: McGraw-Hill, 1973.

JOSÉ DE ARIMATÉIA OLIMPIO FILHO received the B.Sc. degree in electrical engineering from the Federal University of Mato Grosso do Sul, Campo Grande, Brazil, in 2017, and the M.Sc. degree in electrical engineering from São Paulo State University (UNESP), Bauru, Brazil, in 2019.

His main research interests include power electronics and power quality.

Mr. Olimpio Filho was a Finalist in the 2015 IEEE International Future Energy Challenge, was the recipient of the Best Educational Impact Award in MI, USA.

PAULO FERNANDO SILVA received the B.Sc. degree in electrical engineering from Centro Universitário Central Paulista, São Carlos, Brazil, in 2017, and the M.Sc. degree in electrical engineering from the Federal University of São Carlos (UFSCar), São Carlos, Brazil, in 2022. He is currently working toward the Ph.D. degree in electrical engineering from São Paulo State University (UNESP), Sorocaba, Brazil.

He is currently a member of the Automation and Integrated Systems Group (GASI), UNESP. His research interests include modeling and control strategies for power electronic inverters, with an emphasis on microgrids.

LUIS DE ORO ARENAS received the B.S. degree in electronic engineering from the National University of Colombia, Bogotá, Colombia, in 2012, and the M.Sc. and Ph.D. degrees in electrical engineering from São Paulo State University (UNESP), Sorocaba, Brazil, in 2014 and 2019, respectively.

He conducted his postdoctoral studies with the Power Electronics Laboratory, UNESP/FEIS, in 2019, and the Automation and Integrated Systems Group (GASI), UNESP, from 2020 to 2022. He is currently an Assistant Professor with the Department of Environmental Engineering, ICTS, UNESP. His research interests include electronic instrumentation and data science applied to environmental systems, power electronics, power quality, and digital and analog signal processing.

TIAGO DAVI CURI BUSARELLO (Senior Member, IEEE) received the master's and Ph.D. degrees in electrical engineering from the University of Campinas (UNICAMP), Campinas, Brazil, in 2013 and 2015, respectively.

In 2014, he was a Visiting Researcher with the Colorado School of Mines, Golden, CO, USA. He has been a Professor with the Federal University of Santa Catarina, Blumenau, Brazil, since 2016. From 2022 to 2023, he was a Postdoctoral Researcher with the University of Vaasa, Vaasa, Finland. He is also the author of the book *Power Electronic Converters and Systems* (IET, 2024). His research interests include digital control for power electronics and digital twins.

Dr. Curi Busarello is currently a member of the IEEE Power Electronics Society. He is also an Associate Editor for the *Brazilian Journal of Power Electronics*.

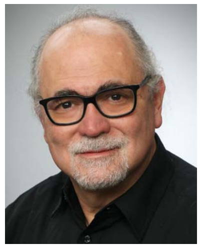

MARCELO GODOY SIMÕES (Fellow, IEEE) received the B.Sc. and M.Sc. degrees from the University of São Paulo, São Paulo, Brazil, in 1985 and 1990, respectively, the Ph.D. degree from The University of Tennessee, Knoxville, TN, USA, in 1995, and the D.Sc. degree (Livre-Docência) from the University of São Paulo, in 1998.

He is a Brazilian American Scientist-Engineer. He holds the title of Emeritus Professor with the Colorado School of Mines, where he served with distinction for 21 years. From 2021 to 2025, he was a Professor "Flexible and Smart Power Systems" with the University of Vaasa, Vaasa, Finland, where he is a Professor Emeritus as well. He has also held long-term faculty positions with the University of São Paulo, plus appointments and short-term visits, research, and teaching in several countries. He was a Fulbright Scholar in Denmark (2014–2015). His research interests include power electronics, power systems, power quality, smart grid, renewable energy systems, and industrial AI applications.

Dr. Simões was recognized for his pioneering applications of artificial intelligence in the control of power electronics systems.

HELMO KELIS MORALES PAREDES (Senior Member, IEEE) received the B.Sc. degree in electrical engineering from San Agustin National University (UNSA), Arequipa, Peru, in 2002, and the M.Sc. and Ph.D. degrees in electrical engineering from the University of Campinas (UNICAMP), Campinas, Brazil, in 2006 and 2011, respectively.

In 2009, he joined the University of Padova, Padua, Italy, as a Visiting Student. In 2014, he joined the University of Nottingham, Nottingham, U.K., as a Visiting Scholar. In 2018, he continued his research abroad as a Visiting Scholar with the Colorado School of Mines, Golden, CO, USA. From 2017 to 2023, he was the Leader of the Automation and Integrated Systems Group (GASI), São Paulo State University (UNESP), Sorocaba, Brazil. Since December 2011, he has been an Associate Professor with UNESP. His research interests include power quality, harmonics and unbalanced propagation, grid-connected converters for renewable energy systems, and microgrid controls.

Dr. Morales Paredes is a member of the Brazilian Power Electronics Society (SOBRAEP) and the Brazilian Automation Society (SBA). He was the recipient the Prize Paper Award from IEEE TRANSACTIONS ON POWER ELECTRONICS, in 2011 and two consecutive Best Paper Awards from Brazilian Power Quality Society (SBQEE) in 2021 and 2023, respectively.

Coordenação de Aperfeiçoamento de Pessoal de Nível Superior (CAPES) - ROR identifier: 00x0ma614